Comprehensive geohazard detection along the Qinghai-Tibet Plateau transportation corridor based on multi-sourced earth observations

Zhenhong Li [a,b,c,d], Chenglong Zhang [a,b,c,*], Chen Yu [a,b,d],
Mingtao Ding [a,b,d], Wu Zhu [a,b,f], Trevor B. Hoey [e], Bo Chen [a,b,f], Jiantao Du [a,b,c],
Xinlong Li [a,b,c], Jianbing Peng [a,b,d]

[a] State Key Laboratory of Loess Science, Chang'an University, Xi'an 710054, China
[b] College of Geological Engineering and Geomatics, Chang'an University, Xi'an 710054, China
[c] Big Data Center for Geosciences and Satellites, Xi'an 710054, China
[d] Key Laboratory of Western China's Mineral Resources and Geological Engineering, Ministry of Education, Xi'an 710054, China
[e] Department of Civil and Environmental Engineering, Brunel University London, Uxbridge UB8 3PH, UK
[f] Key Laboratory of Ecological Geology and Disaster Prevention, Ministry of Natural Resources, Xi'an 710054, China

ARTICLE INFO

ABSTRACT

Geohazards are sudden and catastrophic. Due to the complicated topography, geology and climate conditions along the Qinghai-Tibet Plateau Transportation Corridor (QTPTC), many geohazards pose unprecedented challenges for engineering construction. Comprehensive and scientific geohazard detection has been infrequently performed in the QTPTC, so the study area still lacks a comprehensive geological hazard inventory. With the development of earth observation techniques, detecting geohazards in wide areas is possible. However, comprehensive geohazard detection over such a large spatial extent is considered impossible by individual remote sensing techniques and images. In this study, we used a combination of GACOS-assisted Interferometric Synthetic Aperture Radar (InSAR) phases, SAR amplitudes, and optical images to acquire deformational and geomorphological information of geohazards along the QTPTC. Based on deformational and geomorphological information, we establish a catalogue containing 2109 geohazards which were classified into five categories, i) actively deforming slopes (994); ii) reactivated historically deformed slopes (84); iii) stabilized historically deformed slopes (732); iv) glacier (283) and v) glacial lakes (16). A large percentage of geohazards are distributed at an elevation of 2500–5000 m with slope angles of 30-40°, five geohazards concentration regions are distributed on main active fault zones, and the types of geohazards in the five regions are influenced by precipitation and surface temperature. Finally, three field surveys were also carried out to verify 141 geohazards along the QTPTC. The above findings can improve disaster prevention and mitigation capabilities for construction and operation along the QTPTC.

1. Introduction

The Qinghai-Tibet Plateau Transportation Corridor (QTPTC) starts from Chengdu and terminates at Lasa with a total length of 1800 km. In the QTPTC, geohazards pose great harm to human life and infrastructure, and the landform features deep gorges incising plateaus and hilly basins, with a mean elevation exceeding 3,000 m, gorge relief is predominantly 2,000–3,000 m, reaching a maximum of 5,000 m (Cui et al. 2022). Due to complex topographic settings, there are many kinds of geohazards, especially landslides, for example, on 11 October and 3 November 2018, two massive landslides created a barrier lake in the Jinsha River near the Baige Village, Tibet, causing serious damage to G318 and bridges (Xu et al. 2018). Considering that the study area still lacks a comprehensive geohazards inventory, it is urgent to detect any geohazard that may cause catastrophic consequences and to establish a geohazard catalogue to ensure the long-term safety and reliability of the QTPTC.

At present, Interferometric Synthetic Aperture Radar (InSAR) and optical remote sensing images have been proven to be applicable for landslide detection (Li et al. 2022; Zhang et al. 2022). However,

observing multiple types of geohazards over such a large spatial extent is considered impossible by individual remote sensing techniques. For example, based on optical remote sensing images, Behling et al. (2016) detected 1583 landslides over 2500 km^2 in southern Kyrgyzstan by using optical remote sensing imagery. While optical remote sensing imagery can be used to acquire geomorphological information of stable ancient landslides, due to the influence of low spatial resolution, cloud obstruction, and vegetation cover, optical remote sensing images failed to recognize some active landslides, especially slow-moving ones (Fu et al. 2024). Based on Sentinel-1 images, Zhang et al. (2021c) used InSAR to detect 72 potential active landslides near Wenchuan County, China. However, InSAR may lose coherence if the observed area is covered by heavy vegetation or is moving too fast (e.g., several meters per year). Pixel offset tracking technique with SAR/optical remote sensing images can acquire large gradient surface displacements effectively (Shi et al. 2015), and the Generic Atmospheric Correction Online Service for InSAR (GACOS) is effective in removing atmospheric delay errors (Yu et al. 2017). Both GACOS-assisted InSAR phases and SAR/optical offsets can detect active geohazards (Du et al. 2023), but they do not detect stable ancient slopes despite that they may cause severe damage by sudden collapses (Zhang et al. 2021a). Ground-based SAR can detect geohazards with different gradient rates, and ground-based LiDAR is capable of identifying geohazards with obvious geomorphological information. Airborne optical imagery and LiDAR can acquire a Digital Elevation Model (DEM) within a limited range, and detect geohazards with large gradient surface displacements through the differential analysis of two-phase or multi-phase DEMs. However, the above methods have limited coverage and high costs, making them unsuitable for large-scale geohazard detection. As a result, to comprehensively detect multiple types of geohazards with a high confidence level, an integration of multi-sourced and complementary earth observations is needed (Ge et al. 2019).

In previous research, some scholars have attempted to integrate various Earth observation data into geohazard detection, employing manual visual interpretation or semi-automatic or automatic methods to extract deformational and geomorphological information for study areas based on InSAR results and high-resolution optical remote sensing imagery. For example, Zhang et al. (2022) proposed a wide-area active landslide detection framework with InSAR phases and SAR offsets, and utilized manual visual interpretation to acquire deformational information of landslides in Jinsha River (Li et al. 2022; Zhang et al. 2022). In the Jiuzhaigou area, Cai et al. (2022) used InSAR, LiDAR and optical images to detect 16 slow-moving post-earthquake landslides after the earthquake. Chen et al. (2024) proposed a framework for the wide area detection of active landslides based on SAR and optical images, and used cluster analysis to obtain active landslides (Chen et al. 2024). Fan et al. (2025) developed a spatial context-guided calibration network using multi-source remote sensing imagery to address challenges posed by irregular landslide morphology and environmental interference, thereby enhancing the robustness of landslide detection in complex terrains (Fan et al. 2025). Despite their respective success, there is a lack of research on integrating various Earth observation data into geohazard detection of wide areas such as the QTPTC (over 1800 km). And compared with manual visual interpretation, although semi-automatic or automatic object detection techniques have improved the efficiency of geohazards detection, the detection accuracy of those methods for small-scale landslides remains to be improved, and the generalization capability is poor. So, manual visual interpretation remains an important and effective method for extracting deformational and geomorphological information of geohazards. In addition, previous studies lack a detailed explanation of the distribution patterns of detected geohazards, which can significantly influence our understanding of the mechanisms underlying their occurrence.

In this study, we integrate a combination of Earth observations including ascending and descending C-band Sentinel-1 InSAR phases and SAR offsets, L-band ALOS-2 InSAR phases, and an optical remote

sensing image dataset to comprehensively detect multiple types of geohazards along the QTPTC. This approach can advance the application of multi-source Earth observations in wide-area geohazard detection, and enable the acquisition of the first comprehensive geohazard inventory along the QTPTC. According to the deformational and geomorphological information along the QTPTC, potential geohazards that may cause severe damage to the project can be divided into five categories (Li et al. 2022). We established a comprehensive catalogue containing five types of geohazards and analyzed their distribution in relation to triggering factors such as rainfall and seismogenic faults. Part of the detected geohazards is also validated by three field surveys along the QTPTC.

2. Study area and earth observations

2.1. Study area

The QTPTC serves as one of the vital passageways connecting Tibet with southeastern China, holding significant importance for Tibet's economic development (Fig. 1a). The topographic, geological, and climate conditions of the construction area are greatly complex, passing through eight major mountains, including the Erlang, Zheduo, Hengduan, etc., and seven major river channels, including the Dadu, Xianshui, etc. (Fig. 1b and 1c). The landscape is dominated by deep gorges on plateaus, with an average elevation of more than 3 km and relative elevation differences between 2 and 3 km (Fig. 1c). The stratigraphic in the area is characterized by widely distributed fluvial terraces and segmented by numerous active faults (Xianshuihe, Nujiang and Jinshajiang faults). The climate system is an outcome of interactions among a variety of climate zones, including subtropical monsoon humid, plateau temperate humid, plateau temperate monsoon semi-humid and plateau temperate monsoon dry (Cui et al. 2022; Zhang et al. 2021b). Over 2000 geohazards were reported from 2000 to 2016, among which landslides accounted for 23 %, debris flows for 53.15 % and rock collapses for 19.62 % (Guo et al. 2018; Zhang et al. 2021b). So, the whole QTPTC is an area prone to geohazards.

2.2. SAR data

The Interferometric-Wide Swath (IW) Single Look Complex (SLC) of Sentinel-1 was chosen in this study (Torres et al. 2012). To remove offset caused by topography, the 30 m resolution of the Shuttle Radar Topography Mission (SRTM) Digital Elevation Model (DEM) was used, the coverage of the image is from Chengdu to Lasa (Fig. 2a), and the information about images is shown in Table. 1.

The ALOS-2 satellite was launched on 24 May 2014 and can be used to monitor the Earth's environment and crustal movements. It carries an L-band synthetic aperture radar sensor with strong penetration capacities. In this study, we selected HH polarized SLC images in SM3 mode, covering areas from Yaan to Linzhi (Fig. 2a), and the specific information is shown in Table. 2.

Firstly, the average coherence of Sentinel-1 ascending images (Fig. 2b) and ALOS-2 ascending images (Fig. 2c) is obtained. The sections from Chengdu to Yaan and Ranwu to Linzhi have a high vegetation coverage rate and dense trees (Sun et al. 2020), which leads to a low average coherence, and the coherence of some lakes and glaciers is also low. In the study area, Sentinel-1 and ALOS-2 images are selected for complementary advantages, Sentinel-1 images have the advantages of a short temporal baseline and short spatial baseline, while ALOS-2 images have the benefits of high spatial resolution and long wavelength. Moreover, the study area has strong topography variation and great relative height differences (Cui et al. 2022), so it is necessary to combine different radar satellites and orbit images to avoid the influence of geometrical distortions.
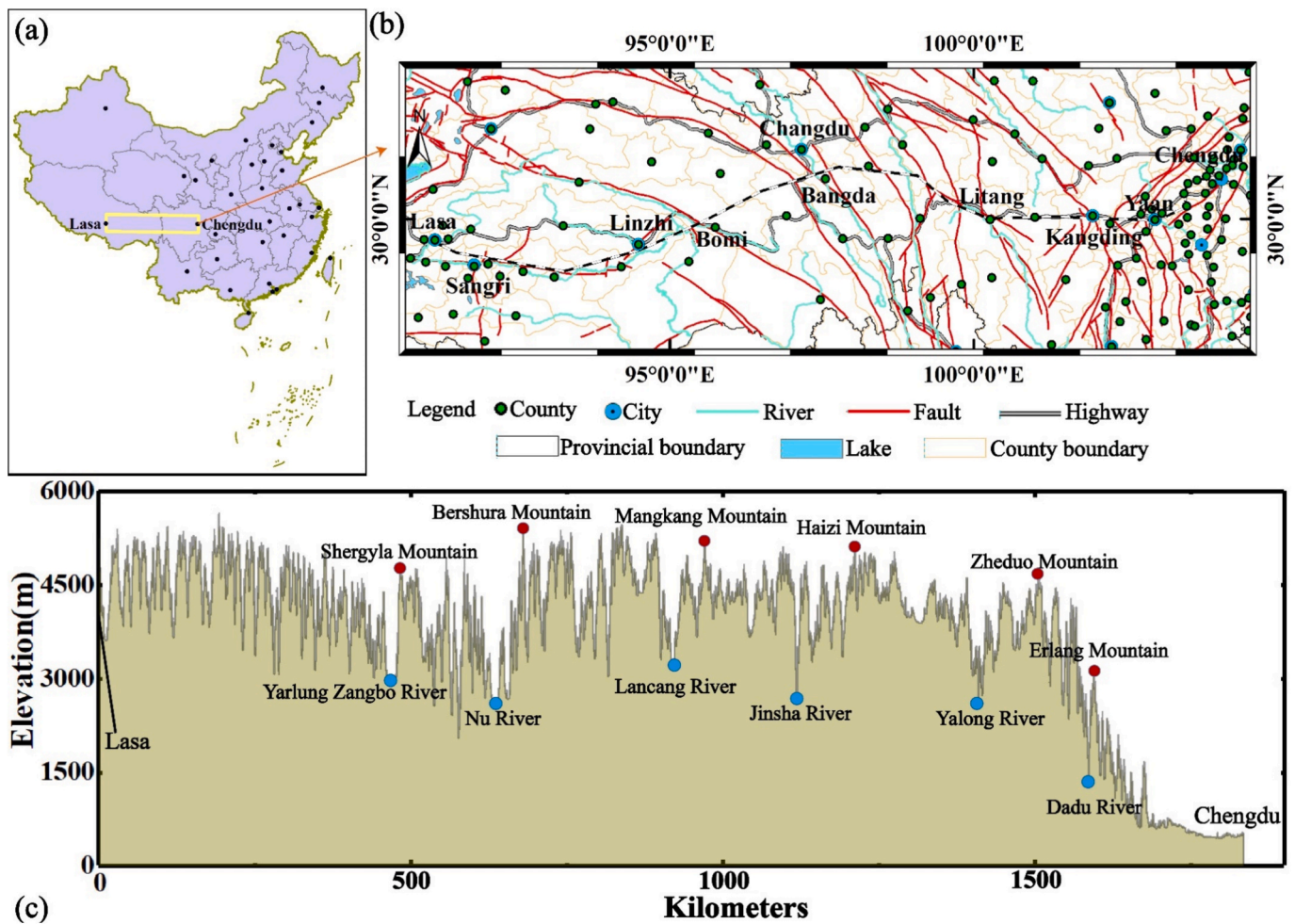
Fig. 1. (a) The geographical location of the study area, (b) the basic information of the QTPTC, and (c) ground elevation along the QTPTC.

2.3. Optical remote sensing data

In this study, optical remote sensing images are provided by Google Earth, a virtual Earth software platform launched by Google in 2005 that mainly includes 3D DEM and global optical remote sensing images. Optical remote sensing images in Google Earth software mainly include high-resolution optical images such as GeoEye-1 (0.5 m), Quickbird (0.6 m) and a small number of SPOT-5 (5 m) images. Most of the images are from 2006 to 2022. All optical remote sensing images used have no cloud cover in research areas, the spatial resolution in the whole research area is better than 5 m, and the image quality can meet the requirements of visual interpretation.

2.4. Other data

SRTM DEM is from the United States Geological Survey (USGS) and the tropospheric delay correction data is from GACOS (Yu et al. 2017). Monthly precipitation data from September 2014 to June 2020 are downloaded from the Global Precipitation Measurement (GPM). Seismic information and seismic Peak Ground Acceleration (PGA) are downloaded from USGS and the Institute of Geophysics, China Earthquake Administration. Surface temperature data are taken from the MODIS11A2 product, which is derived from the Aqua sensor.

3. Methods

In this study, based on SAR (Sentinel-1 and ALOS-2 images) and high-resolution optical remote sensing images, we used GACOS-Assisted InSAR, SAR Pixel Offset Tracking (SPOT) and optical remote sensing visual interpretation to detect geohazards along the QTPTC, and the flowchart is shown in Fig. 3.

3.1. Interferometry

Firstly, SAR images (Sentinel-1 and ALOS-2) and auxiliary data (SRTM DEM, precision orbit, etc.) should be collected, and the SAR images were preprocessed using GAMMA including radiometric calibration, geometric correction and multi-look processing. Sentinel-1 images were processed with 4×1 multilook in distance and azimuth directions, while ALOS-2 images used 2×5 multilook. Then, the master and slave ALOS-2 images were registered at a sub-pixel level (typically with an accuracy of < 0.1 pixel) by matching ground feature points (stable terrain), and platform motion errors were corrected using precise orbit files. Different from ALOS-2 images processing, the acquisition of Sentinel-1 TOPS mode data necessitates more precise image registration because of the antenna's rotation, and registration azimuth accuracy should be higher than 0.001 pixel to avoid phase jump between adjacent bursts (Yagüe-Martínez et al., 2016). For Sentinel-1 SAR images, the temporal and spatial baselines were 60 days and 300 m, respectively. And due to the small number of ALOS-2 images, ALOS-2 images were fully interfered with. Finally, the interferograms were filtered with an adaptive filtering function according to the local fringe spectrum (Goldstein and Werner 1998), and then unwrapped by the Minimum Cost Flow (MCF) algorithm, the coherence threshold was set to 0.3. The 30 m resolution SRTM DEM was adopted to mitigate the influence of terrain (Costantini 1998; Pepe and Lanari 2006).
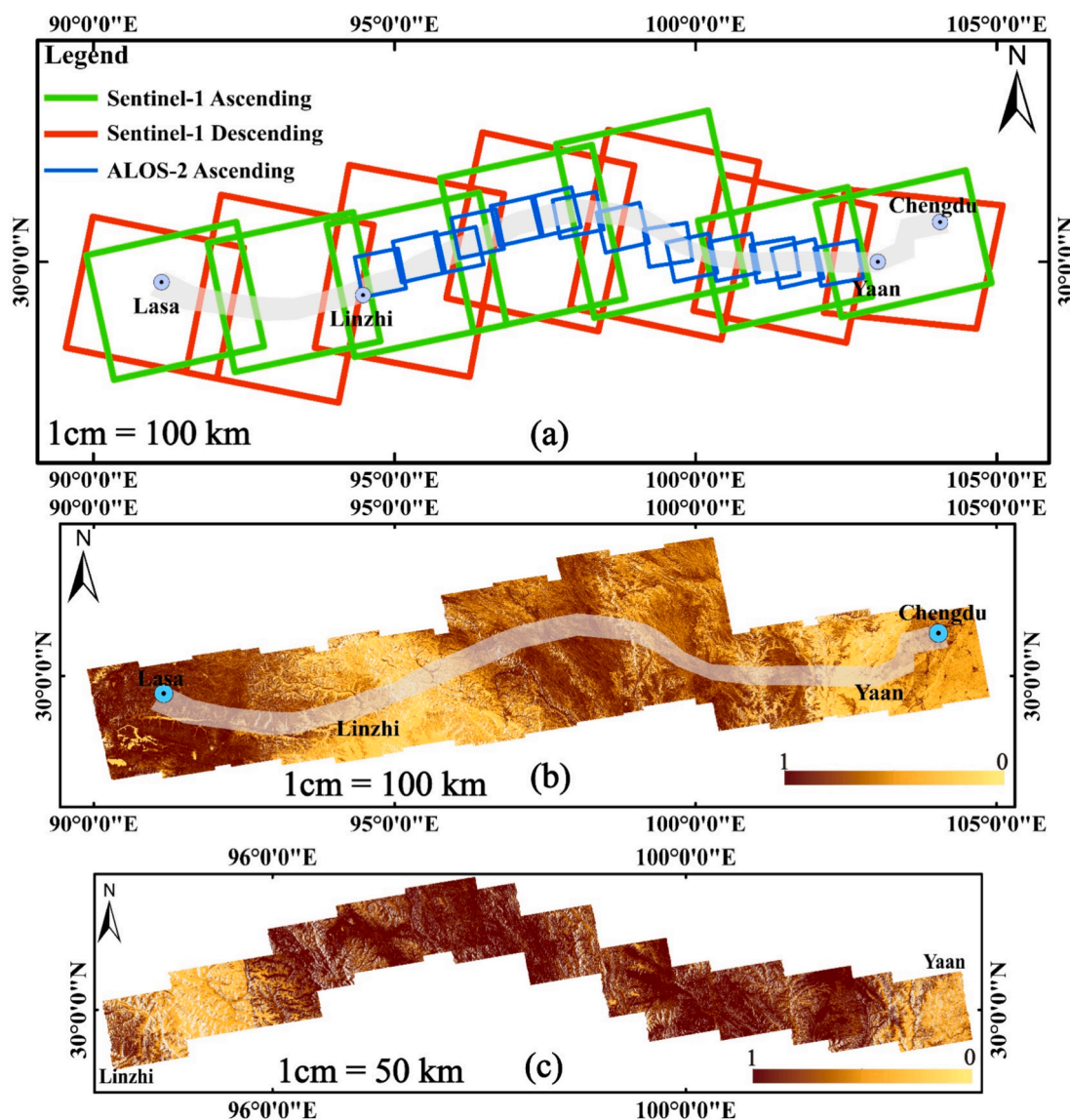
Fig. 2. Study area with the coverage of SAR image dataset: the blue rectangle indicates ascending ALOS-2, the green one ascending Sentinel-1 and the red one descending Sentinel-1(a). The average coherence of Sentinel-1 ascending images and ALOS-2 ascending images: (b) Sentinel-1 ascending images; (c) ALOS-2 ascending images.

Table 1
The information on Sentinel-1 images.

	Path	Start Time	End Time	Images
Ascending	172	2015.04	2019.11	103
	143	2015.07	2019.11	105
	128	2014.10	2019.11	117
	099	2015.01	2019.11	108
	070	2015.01	2019.11	107
	041	2015.01	2019.11	111
	026	2017.11	2019.11	107
Descending	150	2014.10	2020.01	112
	135	2014.10	2020.01	69
	106	2014.10	2020.01	114
	077	2016.06	2020.01	80
	062	2014.10	2020.01	117
	033	2015.08	2020.01	101
	004	2015.05	2020.01	84

Table 2
The information on ALOS-2 images.

|	Path	Beam	Start Time	End Time	Images
Ascending	147	F2-5	2016.02	2020.05	9
	147	F2-6	2016.02	2020.05	8
	148	F2-5	2014.09	2019.05	13
	148	F2-6	2016.07	2020.05	10
	148	F2-7	2016.06	2020.06	11
	149	F2-5	2016.04	2020.05	12
	149	F2-6	2016.02	2020.05	12
	149	F2-7	2016.06	2020.04	9
	150	F2-5	2016.06	2020.05	10
	150	F2-6	2016.07	2020.05	9
	150	F2-7	2016.07	2020.05	8
	151	F2-5	2014.09	2019.09	18
	151	F2-6	2014.10	2019.05	14
	151	F2-7	2014.11	2020.04	11
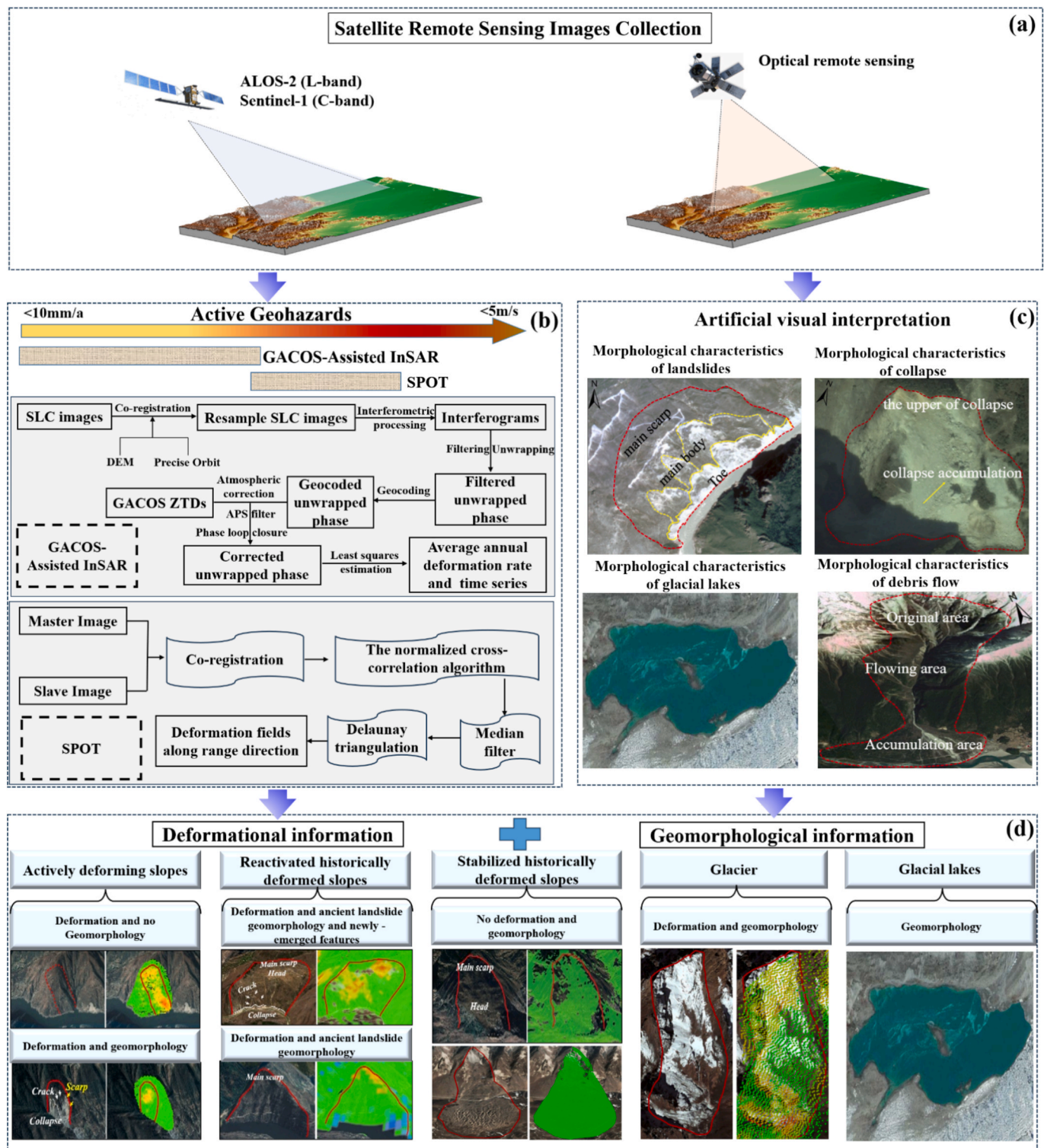
Fig. 3. The flowchart for comprehensive geohazard detection along the QTPTC based on multi-sourced Earth observations.

3.2. GACOS-assisted InSAR

GACOS begun providing global services in June 2017. It is based on High Resolution (HRES) atmospheric model products of the European Centre for Medium-Range Weather Forecasts (ECMWF), with a grid resolution as high as $0.1^\circ \times 0.1^\circ$, and the Iterative Tropospheric Decomposition (ITD) model is used to separate the stratification and turbulence components of the tropospheric delay. Zenith Total Delay (ZTD) images with high spatial resolution (90 m by default) are obtained by spatial interpolation (Yu et al. 2017). GACOS can provide ZTD corrected images from any part of the world for free in near real-time. Researchers can access ZTD products for their study area via email by submitting a form on the official website (https://www.gacos.net) that specifies the location and time range of their research.

The Small-Baseline Subset (SBAS) InSAR technique utilizes SAR interferograms with small baselines to reduce errors in topographic data

and mitigate the effects of baseline decorrelation (Berardino et al. 2002). The advanced SBAS InSAR, which integrates GACOS with a spatial–temporal Atmospheric Phase Screen (APS) filter, was employed to mitigate spatially and temporally correlated atmospheric errors in SAR unwrapped interferograms. Firstly, GACOS was applied to mitigate the elevation-dependent and long-wavelength atmospheric errors in each unwrapped interferogram, and a spatial–temporal APS filter was adopted to further minimize the short wavelength atmospheric errors. Then, phase loop closure was validated by sequentially computing the root mean square (RMS) of the loop closure phase for each unwrapped interferogram. When the loop closure phase error at each pixel exceeds 1.5 rad, the pixel will be masked. Finally, the mean LOS surface displacement rates and time series were determined using least squares estimation (Li et al. 2009; Yu et al. 2020).
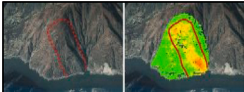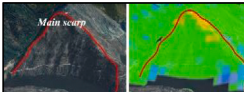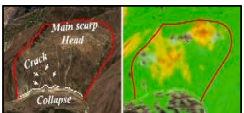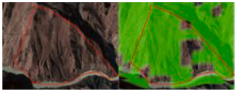
3.3. SAR pixel offset tracking

When applying GACOS-assisted InSAR stacking to process Sentinel-1 datasets, high-spatial-gradient surface displacements could not be detected, and areas with low coherence caused uncertainties in phase unwrapping, leading to potential errors. SPOT technology acquires pixel and sub-pixel level offsets by calculating the correlation between SAR image patches within a search window, thereby tracking moving objects in master–slave images (Leprince et al. 2007; Singleton et al. 2014). SPOT based on intensity information has lower tracking accuracy compared to InSAR and cannot be applied to specific rapid geohazard events, but it can detect large-gradient surface displacements on the decimeter-to-meter scale (Strozzi et al. 2002). In this study, the temporal separation of offset pairs was 30 days. Firstly, in GAMMA software, the master image and slave images were registered with high accuracy. The method calculates offset fields between the master and slave image windows using a normalized cross-correlation algorithm, which is based on the intensity of the SAR images (Huang and Zhen, 2011). The search window and correlation coherence window were 300×60 pixels and 32×32 pixels, respectively, and the cross-correlation coherence threshold was 0.1. Then, considering the accuracy of offset tracking in

range, a median filter with a 9×9 window was applied to reduce the noise. Delaunay triangulation (Pepe and Lanari 2006) was employed to calculate the spatial correlation of pixel offset pairs. If the offset differences of 80 % of neighboring pixels exceed 0.5 pixels, the pixels are classified as noise, otherwise, they are identified as real ground movements. Finally, the range offset map was obtained. Due to the limited accuracy of surface deformation measurements in the azimuth direction of Sentinel-1 SAR, only the range offset was utilized.

3.4. Visual interpretation

Artificial visual interpretation is still one of the main methods for geohazard detection in some wide-area areas by using optical remote sensing images. In this study, artificial visual interpretation was used along the QTPTC, actively deforming slopes, reactivated historically deformed slopes and stabilized historically deformed slopes, glaciers and glacial lakes are the main geohazards. Glaciers and glacial lakes can be easily identified visually (Fig. 3d), and for slopes, visual interpretation can use optical remote sensing images to obtain many features of landslides such as shape, tone and texture, and then combine with landslides identification mechanism for analysis and inference (Othman and Gloaguen 2013; Zhuang et al. 2018). By analyzing the spectral and textural differences in optical images taken at different times, along with topographic features, reactivated historically deformed slopes, actively deforming slopes and stabilized historically deformed slopes can be preliminarily interpreted, of course, deformational information needs to be combined to determine (Fig. 3d and Table.3). Actively deforming slopes are areas that are currently undergoing deformation and have obvious deformational characteristics, the main interpretive signs are cracks, scarps and collapses on slopes. Reactivated historically deformed slopes are landslides that occurred in the past and are still deforming. Their main interpretive features include relatively complete landslide characteristics, such as a main scarp, foot, main body and toe, etc. Due to ongoing deformation, obvious cracks are present on the main body, with vegetation differences compared to the surrounding areas. Stabilized historically deformed slopes refer to landslides that occurred in the past

Table 3
. Landslide categorization and detection methods.

Landslide Types	Examples	Features	Detection Methods
Actively deforming slopes (I)		Deformation, with no Geomorphological features	InSAR, SPO and optical image interpretation
		Deformation, with geomorphological features (cracks, scarps and collapses)	InSAR, SPO and optical image interpretation
Reactivated historically deformed slopes (II)		Deformation and Landslide features (main scarp, main body, foot and toe)	InSAR, SPO and optical image interpretation
		Deformation, Landslide features (main scarp, main body, foot and toe), and newly added cracks and scarps	InSAR, SPO and optical image interpretation
Stabilized historically deformed slopes (III)		Landslide features (main scarp, main body, foot and toe) and no Deformation	Optical image interpretation
Undeformed but potentially unstable slopes collapses (IV)		No deformation orgeomorphological feature	Geophysical prospecting technology

and are currently stable condition (Xu et al. 2022). The only difference in interpretive features between this kind of landslide and reactivated historically deformed slopes is the absence of deformation signs (Li et al. 2022).

3.5. Comprehensive detection of geohazards

The deformational information acquired by InSAR and SPO and geomorphological information acquired by optical remote sensing visual interpretation, were utilized to classify geohazards. It should be noted that in this study, for active slopes, those with a deformation rate greater than |10| mm/year and an area exceeding 0.04 km^2 are defined
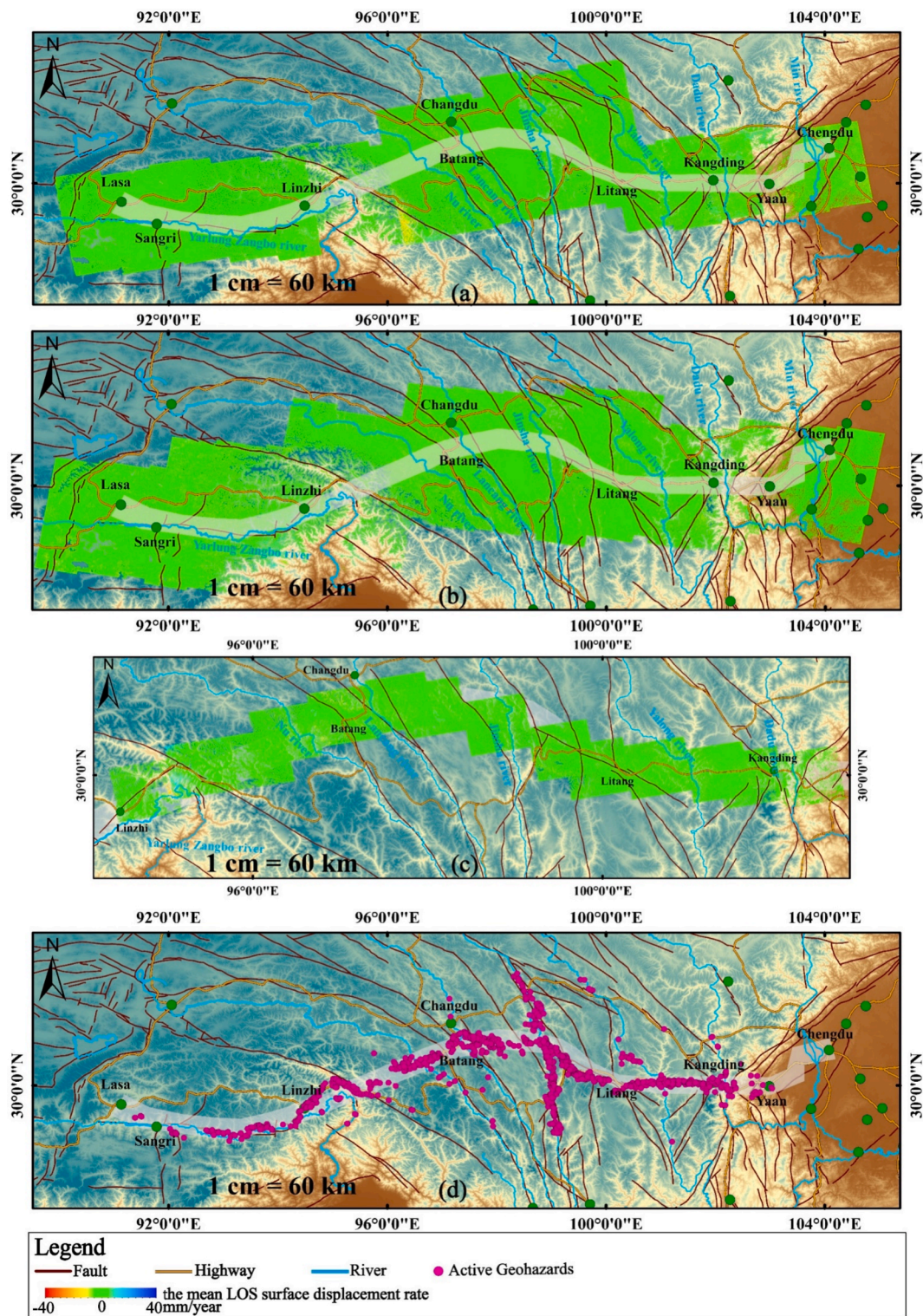

Fig. 4. The mean LOS surface displacement rates by GACOS-assisted InSAR stacking: (a) Sentinel-1 descending, (b) Sentinel-1 ascending, (c) ALOS-2 ascending, (d) active geohazards distribution map.

as hazards, and for stabilized historically deformed slopes, those with an area greater than 0.04 km^2 are defined as hazards. As mentioned above, glaciers and glacial lakes can be easily identified visually. For slopes, however, based on these two types of information, they are categorized into three types: actively deforming slopes, reactivated historically deformed slopes and stabilized historically deformed slopes (Table. 3). Actively deforming slopes has no historical landslide occurrences and lack characteristic landslide features such as main scarp, main body, foot and toe. They are currently undergoing persistent deformation, and may exhibit surface deformation signs such as cracks and scarps. Type I is mainly divided into two cases: one is in the slow deformation station, where InSAR technology can detect deformation but no obvious deformation signs are visible in optical remote sensing images. The other involves relatively obvious deformation, with clear signs (cracks and scarps) in optical remote sensing images. Reactivated historically deformed slopes have experienced landslides in history, show typical landslide morphological features (main scarp, main body, foot and toe) and deformation signals, and may exhibit morphological signs such as the newly added cracks and scarps. Type II is further subdivided into two scenarios: one is characterized by both deformation and typical landslide characteristic information (main scarp, main body, foot and toe). The other involves deformation signals, typical landslide characteristic, and newly formed cracks and scarps. Stabilized historically deformed slopes only exhibit typical landslide morphological features (main scarp, main body, foot and toe) with no deformational information. However, Type IV landslides lack both geomorphological and deformational information, and can't be detected by InSAR or optical remote sensing data. They can be identified based on their geological structures and geophysical prospecting technology, but these methods are unsuitable for wide-area detection due to high implementation costs (Chen et al. 2022; Li et al. 2022).

4. Results

4.1. Geohazards detected by GACOS-assisted InSAR

The mean LOS surface displacement rates of the study area were obtained by GACOS-Assisted InSAR (Fig. 4a-4c). If the study area has large relative height differences, geometric distortions such as layover and shadow are likely to occur, thus, multi-source SAR images should be used for comprehensive analysis. Since the wavelength of ALOS-2 images is much longer than Sentinel-1 images, ALOS-2 images can identify slopes missed in the incoherence areas of Sentinel-1 data. It also plays a significant role in detecting some new/ancient landslides (actively deforming slopes/reactivated historically deformed slopes) with dense vegetation coverage or very slow deformation. In Fig. 4, deformation
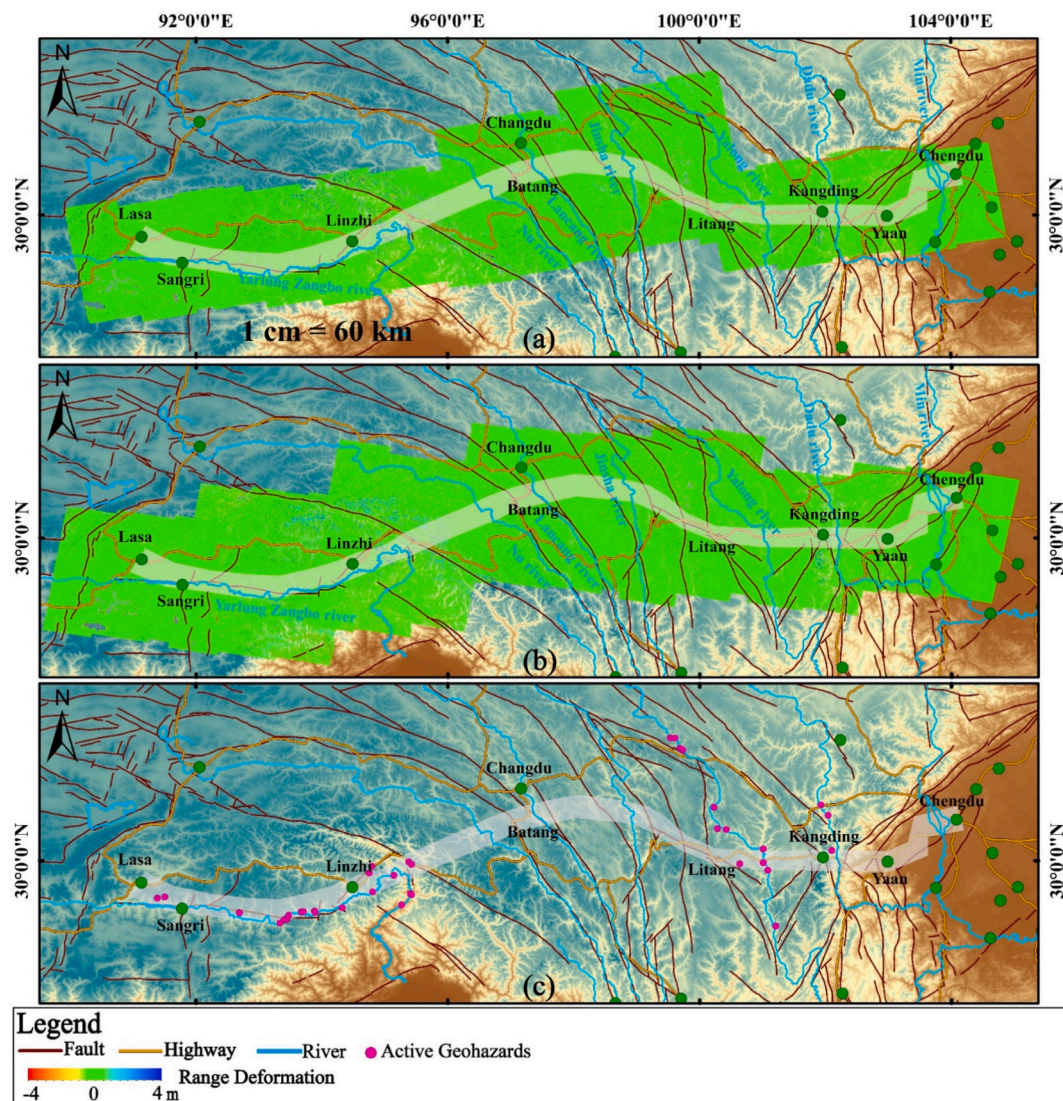

Fig. 5. Range direction deformation by SPO: (a) Sentinel-1 ascending, (b) Sentinel-1 descending. (c) Active slopes distribution map.

occurs in many areas, with 1237 active geohazards detected (Fig. 4d). The number of deformation areas gradually increases from east to west along the QTPTC. Higher elevation differences provide favorable external conditions for the formation of active geohazards, while greater temperature differences reduce slope ductility and intensify glacial movement, thereby promoting the occurrence of active geohazards.

4.2. Geohazards detected by SPOT

Using GACOS-Assisted InSAR for wide-area detection, when active slopes undergo large gradient surface movements over a relatively short period, severe incoherence occurs in these regions, making InSAR technique unable to detect some active slopes. To address this issue, we used SPOT to process Sentinel-1 and obtained the range direction deformation (Fig. 5). There are thirty-six active slopes with large gradient surface movements along the QTPTC, mainly distributed in the Dadu River, Jinsha River River and Linzhi to Lasa section.

4.3. Geohazards detected by optics remote sensing

In Google Earth, multi-temporal high-resolution optical remote sensing images were used to interpret the study area visually, and 1254 geohazards were detected, of which 872 geohazards (Fig. 6a) were not detected by InSAR and SPOT. In Fig. 6b, the optical remote sensing image on October 11, 2020 was acquired by GaoFen-2 with 3.24 m spatial resolution, it shows a typical creeping rock landslide (30.57°N, 98.92°E) with main scarp, toe and main body of a landslide. In Fig. 6c and 6d, the optical remote sensing data, sourced from Google Earth, represent a collapse and a debris flow, respectively. The collapse in Fig. 6b is a geological phenomenon in which rocks on the steep slope suddenly broke away from the parent body under the action of gravity and collapse, rolled and accumulated at the slope foot. The main indicators of collapses include steep, mostly composed of hard rocks with light-colored joints and fissures. The upper part of collapses is often unvegetated, while the lower part has gentle slopes with loose accumulations prone to collapse, and the surface of collapses is rough and clear boundaries. The debris flow in Fig. 6d is a special torrent carrying large amounts of mud and rocks, triggered by heavy rains, snowstorms, glaciers or other natural disasters. It mainly includes the original area,

flowing area and accumulation area. The main influencing factors of debris flow formation include historical factors, topographic factors, geological factors, rainfall factors, surface cover, etc. The QTPTC extends the eastern Sichuan Basin to the western Qinghai-Tibet Plateau, with glaciers becoming increasingly widespread from east to west. This provides necessary conditions for the occurrence of glacial debris flows and glacial lake (Fig. 6e) outburst floods.

4.4. Integrated detection results

As shown in Fig. 7, 2109 geohazards were detected. Based on deformational and geomorphological information, geohazards were divided into five types: actively deforming slopes, reactivated historically deformed slopes, stabilized historically deformed slopes, glaciers and glacial lakes. Geohazards are mainly distribute in the Dadu River, Xianshui River, Yalong River, Jinsha River, Lancang River and Yarlung Zangbo River. There are 47 % (994) actively deforming slopes, 4 % (84) reactivated historically deformed slopes, 35 % (732) stabilized historically deformed slopes, 13 % (283) glaciers, and 1 % (16) glacial lakes.

SAR and optical remote sensing images were complementary in geohazard detection. Radar remote sensing can obtain slopes and glaciers with specific deformational information, especially for some slopes that are difficult to detect by optical remote sensing due to very slow deformation. Optical remote sensing can give full play to detect some stabilized historically deformed slopes (i.e., ancient landslides) and large gradient deformation similar to the Baige landslide where SAR images are incoherent. However, it should be noted that incoherence induced by large-gradient deformation will cause missed detections by InSAR technology, in this case, SPOT technology can be used as a supplement, and multi-temporal optical remote sensing imagery can be used to detect slopes and glaciers with distinct morphological characteristics. Therefore, by using InSAR, SPOT and visual interpretation technologies in a complementary manner, the comprehensive utilization of multi-source remote sensing datasets can effectively improve the accuracy, reliability and completeness of geohazard identification.
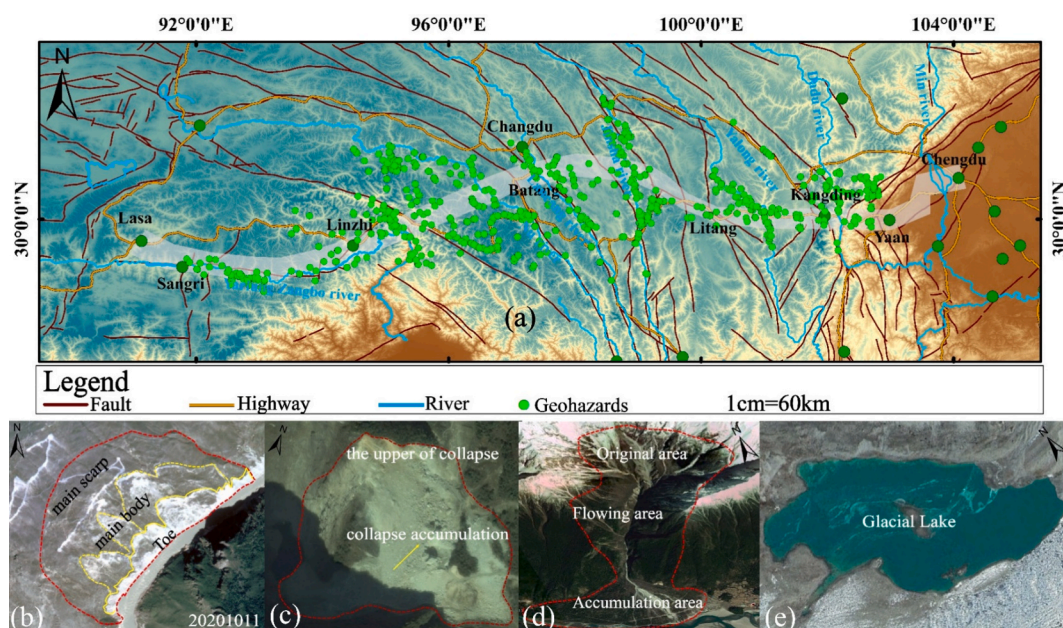

Fig. 6. (a) Optics remote sensing detection results of geohazards, landslides and a glacial lake: (b) (30.57°N, 98.92°E); (c) (30.48°N, 102.73°E); (d) (29.92°N, 95.44°E); (e) (29.05°N, 94.00°E).
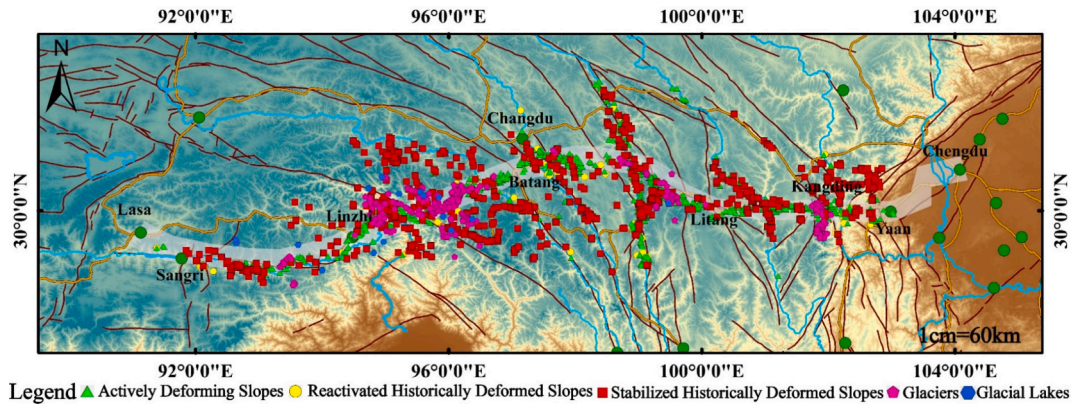
Fig. 7. Geohazards distribution along the QTPTC. The green triangle indicates actively deforming slopes, the yellow circle indicates reactivated historically deformed slopes, the red rectangle indicates stabilized historically deformed slopes, the pink pentagon indicates glaciers, and the blue hexagon indicates glacial lakes.
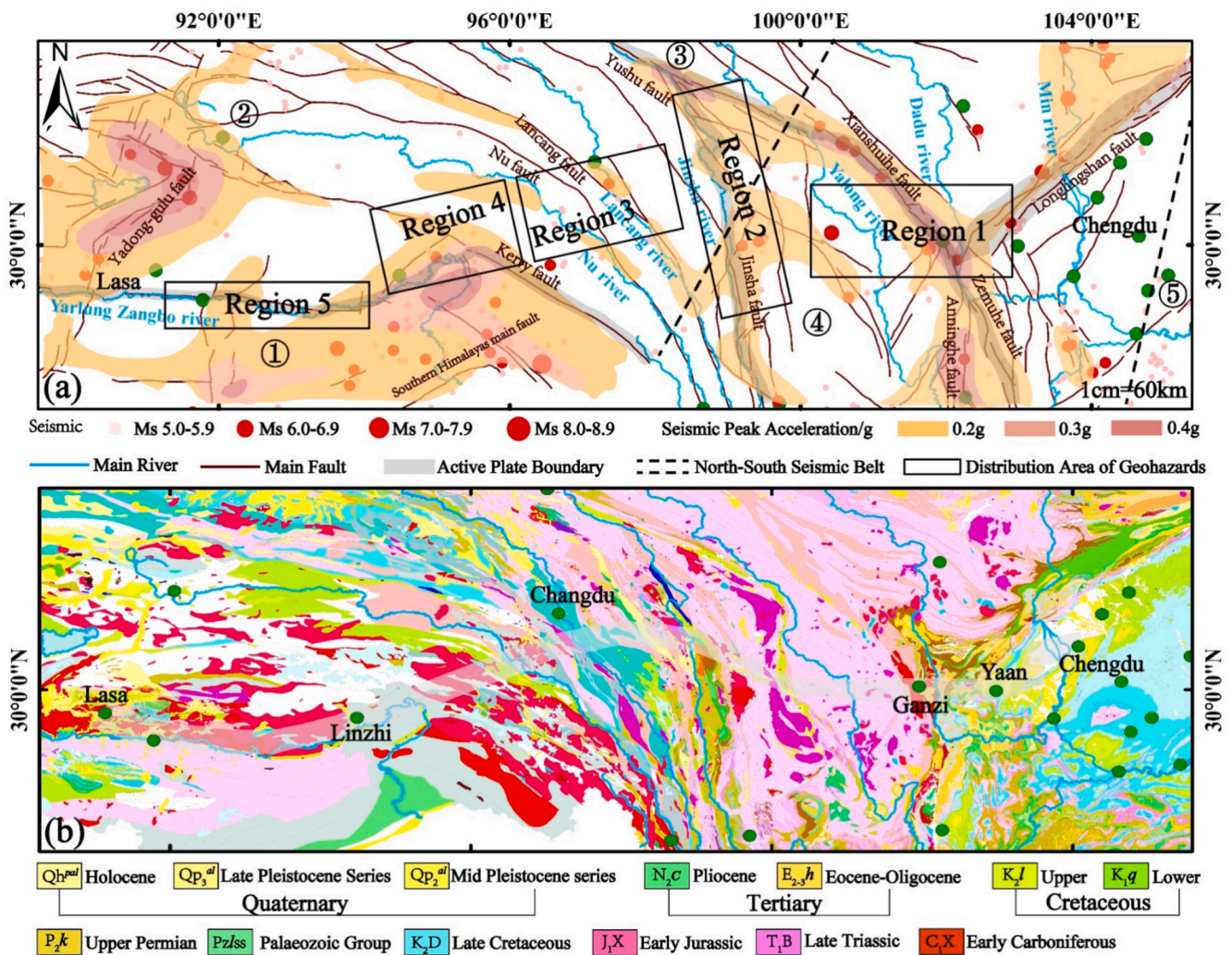

Fig. 8. (a) Major active tectonic regions, active fault zones and seismic PGA distribution map: ①Himalayan Plate, ②Tibet Plate, ③Gansu-Qinghai Plate, ④Sichuan-Yunnan Plate, ⑤South China Plate. (b) Lithology distribution map (1:50000).

5. Discussion

5.1. Distribution regularities of geohazards

5.1.1. Internal factors of the study area

As shown in Fig. 8a, the study area is located east of the Tibetan

Plateau, so the geological characteristics and tectonic settings of this area are closely related to the tectonic evolution of the Tibetan Plateau. Several important active tectonic faults (Xianshuihe fault and Jinshajiang fault) divide it into four main tectonic plates: the Tibetan Plate, Himalayan Plate, Gansu-Qinghai Plate and Sichuan-Yunnan Plate. The Yarlung Zangbo Suture zone is the boundary between the Himalayan

Plate and Tibetan Plate, and the Jinshajiang fault is the boundary between the Tibetan Plate and Gansu-Qinghai Plate, as well as the southwest boundary of the Sichuan-Yunnan Plate, the Xianshuihe fault is the northeast boundary of the Sichuan-Yunnan Plate. There are several areas in the study area with PGA greater than 0.2 g, reaching 0.3 g in Kangding-Daofu and Bomi-Linzhi-Milin areas, and some regions in Kangding and southeastern Linzhi even exceeding 0.4 g. Especially, in the Batang, Litang and Kangding areas along the Jinshajiang fault zone and Xianshuihe fault zone, frequent seismic activity can not only lead to mountain loosening but also directly trigger geohazards. Fig. 8b shows the lithology distribution map (1:50,000) of the study area, the distribution of lithology is controlled by geological structure, and the orientation of lithology is basically the same as that of regional controlling fault, which runs North-South from Chengdu to Bomi, and gradually becomes East-West from Bomi to Lasa. The stratigraphy of the study area is complex and dominated by sedimentary rocks, mainly including Quaternary, Tertiary, Cretaceous, Upper Permian, Palaeozoic Group, Early Jurassic, Late Triassic and Early Carboniferous.

The distribution of geohazards detected is closely related to geological characteristics and tectonic settings of the study area. Tectonic activities can break up rocks to form physical sources of geohazards and cause terrain steepness to form topographic conditions of geohazards. Geohazards are widely distributed on the boundaries of active plates, and we have divided the study area into five parts (geohazards concentration areas) based on the distribution of active fault zones. Region 1 is dominated by the Xianshuihe fault, Zemuhe fault and Longlingshan fault, where earthquakes of magnitude Mw 7.0 and above have occurred. The dominant lithology here is granite. The Jinsha fault and Yushu fault are mainly distributed in region 2, which mainly includes the Jinshajiang suture zone and Maoyaba area, the lithology mainly includes limestone, sandstone, phyllite, diorite and granite. Region 3 is dominated by the Lancangjiang fault and Nujiang fault, geohazards are widely distributed in the suture zones of the Lancang and Nu rivers, and lithology consists mainly of clastic rock, sandstone, gneiss, marble and granite. Regions 4 and 5 are located on the Himalayan and Tibet Plates, dominated by the Kerry fault and Southern Himalayas main fault. The Himalayan Plate is prone to earthquakes of magnitude Mw6.0 and above, including one of magnitude Mw 8.6, and region 5 is also influenced by the Yadong-gulu fault, making geohazards widespread along the Yarlung Tsangpo suture zone. The lithology of region 4 consists mainly of clastic rock, granite, marble, limestone and volcanic rock, while the lithology of region 5 consists mainly of granite, marble, limestone, clastic rock and arenaceous-shale. In short, active tectonic zones, river suture zones and lithology within Tibetan Plateau affect the spatial distribution of geohazards.

5.1.2. External environments of the study area

External environments of the study area are mainly topography and driving factors. Topography is one of the main controlling factors in geohazard formation, topographic factors, including ground elevation, slope and aspect, are key factors in the occurrence of slopes and affect distance, direction, speed and coverage of slope movement. Ground elevation data were derived from SRTM DEM with 30 m resolution, and slope and aspect were calculated in ArcGIS based on SRTM. Precipitation and surface temperature are the primary triggers of geohazards.

In general, the number of geohazards initially increases and then decreases as ground elevation increases, the proportion of geohazards with elevation values between 2500–5000 m is 86.5 %, which is conducive to the occurrence of geohazards (Fig. 9a). As shown in Fig. 9b, the overall trend of geohazards with changes in aspect is not obvious, indicating that sensitivity of geohazards to aspect is relatively low. In Fig. 9c, the number of geohazards initially increases and then decreases with higher slope values, in the slope interval of 30-40°, the distribution of geohazards is high density, accounting for 66.4 %, which is conducive to geohazard occurrence. The slope of terrain affects the distribution of precipitation, which in turn affects vegetation coverage, and slopes directly affect dynamic conditions for geohazards initiation, higher slopes are favorable for geohazards initiation. However, excessively steep slopes hinder the accumulation of geohazard sources, leading to a low frequency of geohazards. In summary, the number of geohazards along the QTPTC is influenced by ground elevation and slope.

Fig. 10 shows the total precipitation along the QTPTC from September 2014 to June 2020. Water is one of the most active dynamic factors in the development of geohazards, rainfall, river erosion, irrigation and action of groundwater all influence the formation and distribution of geohazards. Precipitation not only increases the self-weight of soil mass and sliding thrust but also transforms into groundwater, generating infiltration forces that lubricate and soften sliding surfaces, which is extremely detrimental to the stability of loose soil slopes. Fig. 11a and 11b show the average surface temperature at 13:30 in the study area for January − March 2020 and July − September 2020, respectively, Fig. 11c shows the average surface temperature at 13:30 from September 2014 to June 2020 along the QTPTC. Surface temperature is another important driving factor, due to the existence of water, large temperature differences seriously affect the volume change of the slope body, resulting in the freeze-thawing phenomenon, and leading to instability of the slope, especially in case of extreme cold, it is easy to cause glacial lake outburst floods.

In order to analyze the distribution of geohazards, we have classified five types of geohazards into a secondary category including collapses, debris flows, ancient landslides, freeze-and-thaw weathering landslides, shallow landslides, unstable slopes, glaciers, glacial lake outbreaks and creeping landslides (Note: the order represents the priority of classification). Glaciers are predominantly found in regions 1 and 4, which are located in high altitudes with heavy rainfall of over 4000 mm and low surface temperatures, below −10 °C throughout the day in winter. Collapses are mainly distributed along the sides of rivers, especially along the Yalong and Yarlung Zangbo Rivers, where rainfall is greater
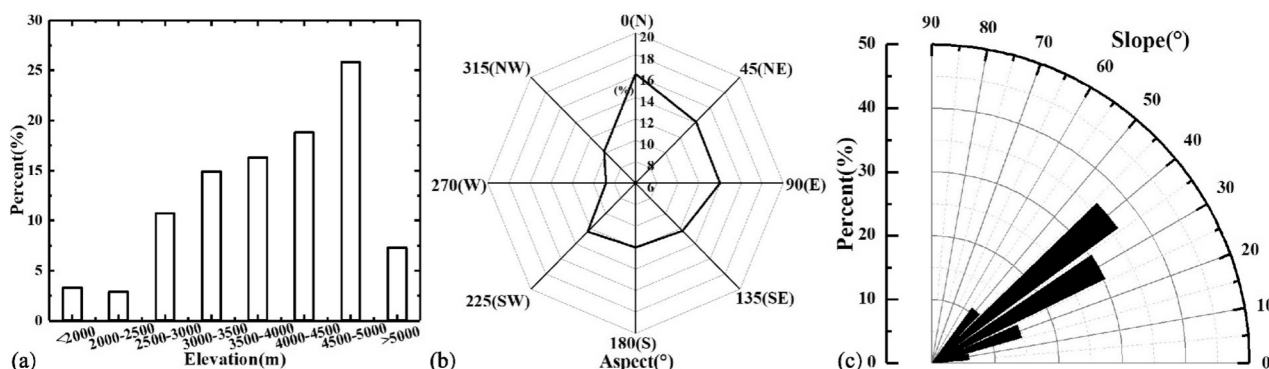

Fig. 9. Statistics analyses of geohazards distribution: (a) ground elevation, (b) aspect and (c) slope.
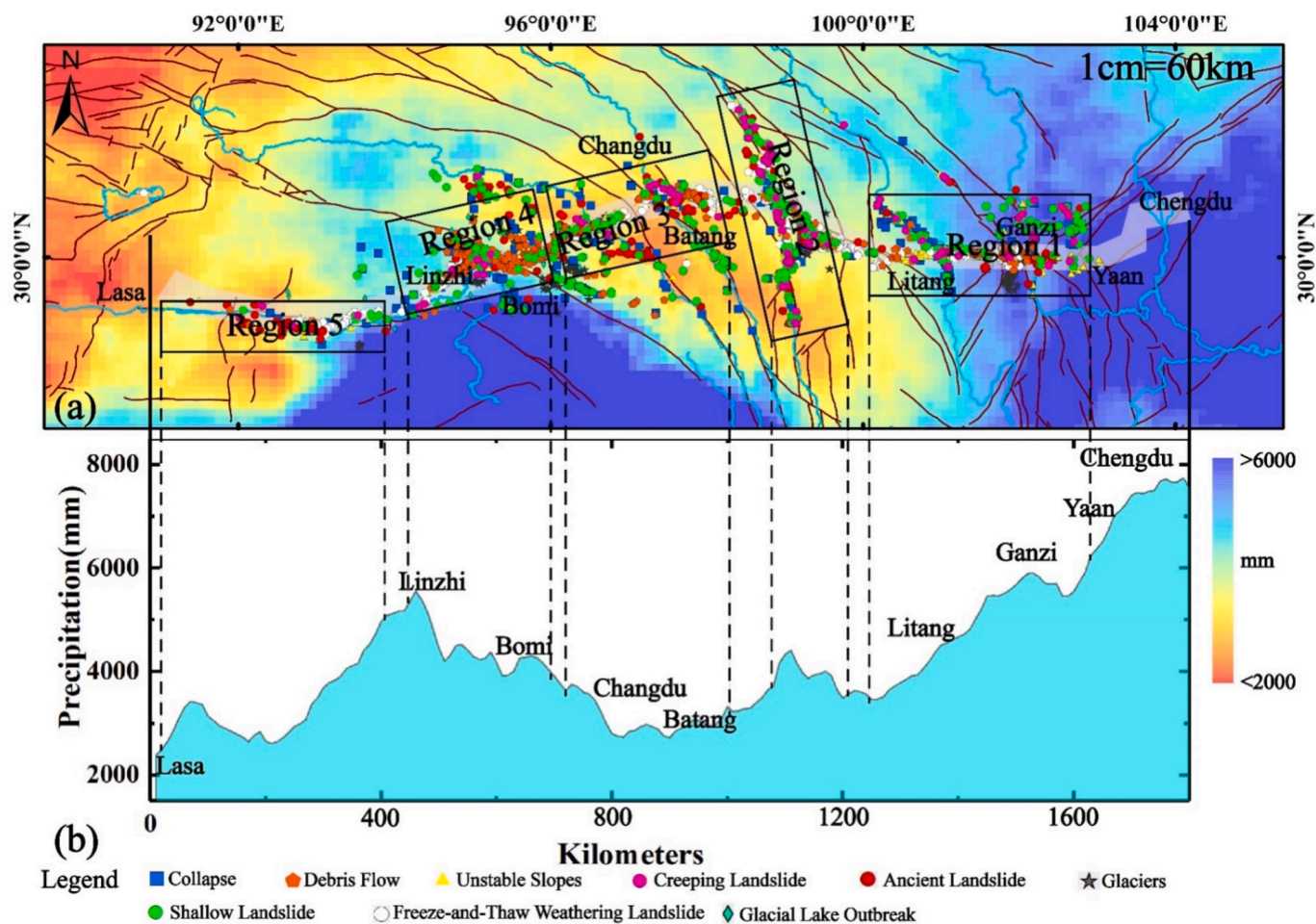
Fig. 10. (a) Cumulative precipitation in the study area between September 2014 and June 2020, (b) total precipitation from September 2014 to June 2020 along the QTPTC. The blue rectangle indicates collapses, the orange pentagon indicates debris flows, the yellow triangle indicates unstable slopes, the pink circle indicates creeping landslides, the red circle indicates ancient landslides, the green circle indicates shallow landslides, the white circle indicates freeze-and-thaw weathering landslides, the black star indicates glaciers, the cyan-blue diamond indicates glacial lakes outbreak.

than 4000 mm, the surface temperature is lower and slopes are less resilient, making them prone to instability damage and falls. Some landslides are widely distributed along the QTPTC, creeping landslides, shallow landslides and ancient landslides are mainly distributed in region 2, where precipitation is 3000–4000 mm and the surface temperature difference is about 20 degrees. In addition, tectonic activities and lithology characteristics mentioned above in this region lead to the widespread distribution of geohazards. Freeze-and-thaw weathering landslides are mainly distributed in regions 3, 4 and 5, with precipitation of 3000–5000 mm and a surface temperature difference of more than 15 degrees, in some areas of region 4, the surface temperature difference reaches 25 degrees. It is worth noting that some areas of region 4 have subzero surface temperatures all year round, with an average surface temperature of $-19\ ^{\circ}\text{C}$ at 13.30 in the winter months of January to March and that the abundance of rainfall (over 4,000 mm) has resulted in debris flows and glacial lakes outbreaks flood being more widespread in this region. In summary, the types of geohazards in the five regions are influenced by precipitation and surface temperature.

5.2. The influence of geohazards along the QTPTC

In the study, the QTPTC was divided into 16 sections from Lasa to Chengdu. In Fig. 12a and 12b, areas with high geohazard density are all concentrated in river basins. The geohazard densities in the 11th, 7th and 10th sections exceed $24*10^{-3}$ points/km^2, reaching $30.84*10^{-3}$ points/km^2, $26.78*10^{-3}$ points/km^2, and $24.53*10^{-3}$ points/km^2, respectively. The highest geohazard density is distributed in the Jinsha River Basin(11th). Fig. 12c shows geohazard density versus distance along the QTPTC. The geohazard density decreases progressively with distance from the QTPTC over the range of 0 to 30 km, with the highest density of $19.03*10^{-3}$ points/km^2 observed within 5 km of the corridor.

In Fig. 13a, the boundaries of all slopes based on deformational and geomorphological information were drawn, according to the harm of slopes to the QTPTC, twenty-eight typical slopes were selected for detailed analysis (Fig. 13b), Fig. 13b not only shows the mean LOS surface displacement rate of slopes, but also obvious geomorphological characteristics in optical remote sensing images. Twenty-eight slopes are distinguishable. For example, in Fig. 13b − (23), it is a typical creeping landslide (an actively deforming slope) that the area is 3 km^2, and the maximum mean LOS surface displacement rate is − 82 mm/year, through optical remote sensing data, it can be judged that this landslide is a rock landslide, with rocks at the upper edge, many scarps at the main body and obvious sliding in the lower edge of the landslide. Fig. 13b − (27) illustrates a typical reactivated ancient rock landslide (a reactivated historically deformed slope) featuring accumulation layers and an armchair shape, with significant surface displacements observed in the main scarp (−70 mm/year) and the main body (−80 mm/year). Fig. 13b − (45) is a shallow landslide (actively deforming slopes), with small deformation on the slope surface, and no obvious geomorphological characteristics of this landslide are visible in the optical image, the
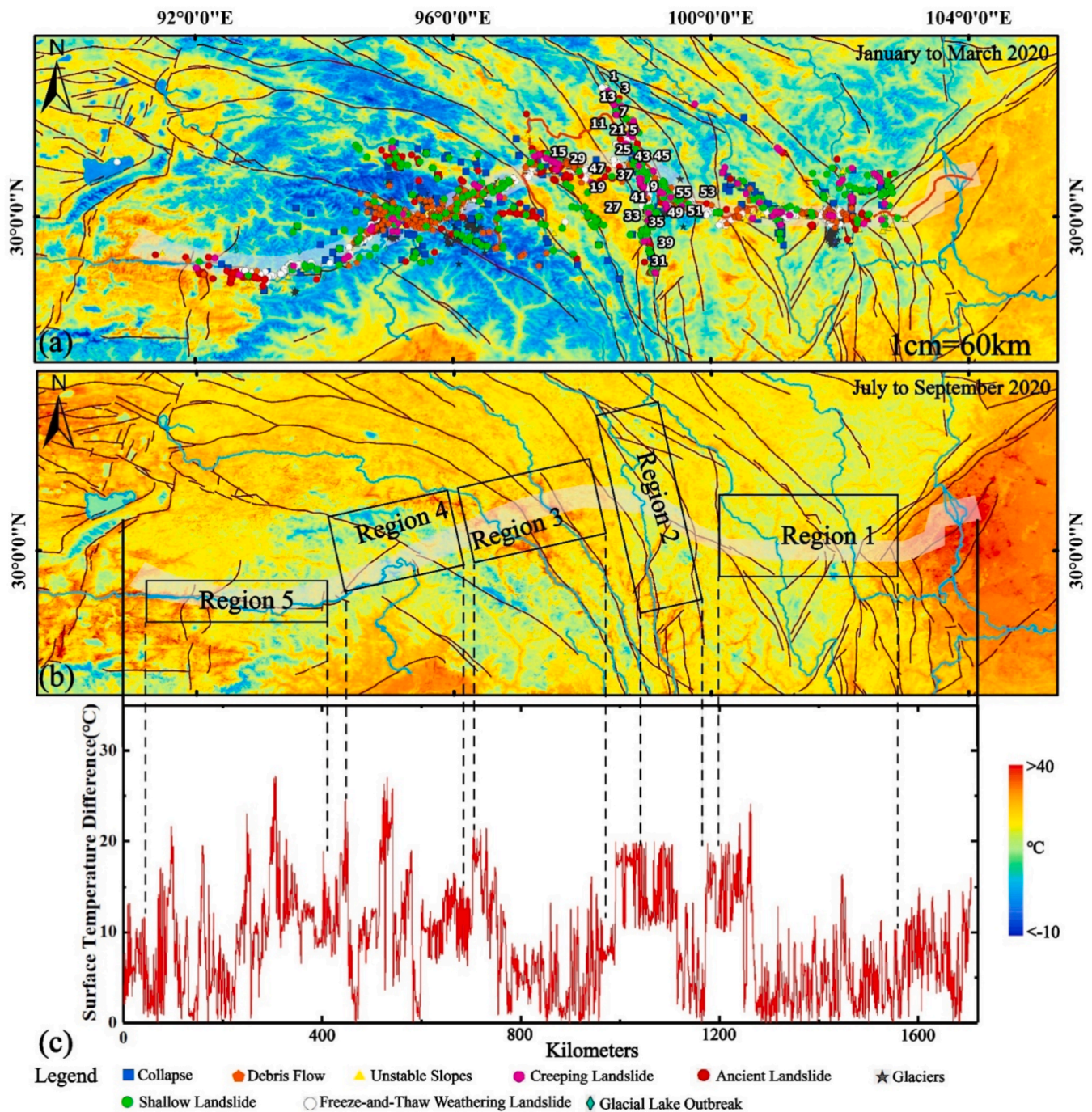
12

Fig. 11. (a) The average surface temperature in the study area at 13:30 from January to March 2020, (b) the average surface temperature in the study area at 13:30 from July to September 2020, (c) the average surface temperature difference at 13:30 from September 2014 to June 2020 along the QTPTC.

maximum mean LOS surface displacement rate is smaller (12 mm/year) than other types of slopes, and the area deformation is also small (1.5 km^2). Fig. 13b − (51) is a debris flow (actively deforming slopes) with many deformation areas in this region, the maximum mean LOS surface displacement rate is −59 mm/year. Along the QTPTC, particularly in the permafrost regions with high altitude and great topographic relief, there are many freeze-and-thaw weathering landslides. In Fig. 11b − (53), it is a typical freeze-and-thaw weathering landslide group (actively deforming slopes), from the optical image, it is clear that the terrain in this area is elevated and steep, gentle slopes alternate with steep ridges, ice and snow accumulate in gentle slope sections, the supporting effect of steep slopes is reduced, and freeze-and-thaw weathering landslides

are prone to occur, the maximum mean LOS surface displacement rate is −65 mm/year.

The first landslide (an actively deforming slope) is a typical creeping rock landslide located at Zhongdui Village, Lieyi Township, Batang County, Sichuan Province, the distance from the landslide to the QTPTC is about 2.3 km. It can be seen from Fig. 14a that the mean LOS surface displacement rate of a large area exceeded −10 mm/year, the LOS surface displacement time series of pixel points P1 and P2 reached −36 mm and −96 mm, respectively (Fig. 14e). The upper edge of the landslide is deformed obviously, during the period from June 2018 to June 2019, the LOS surface displacement time series at the pixel point P2 was significant, and then the deformation became slow, and started to accelerate at P1 in June 2020 (Fig. 14e). In Fig. 14f, the LOS surface
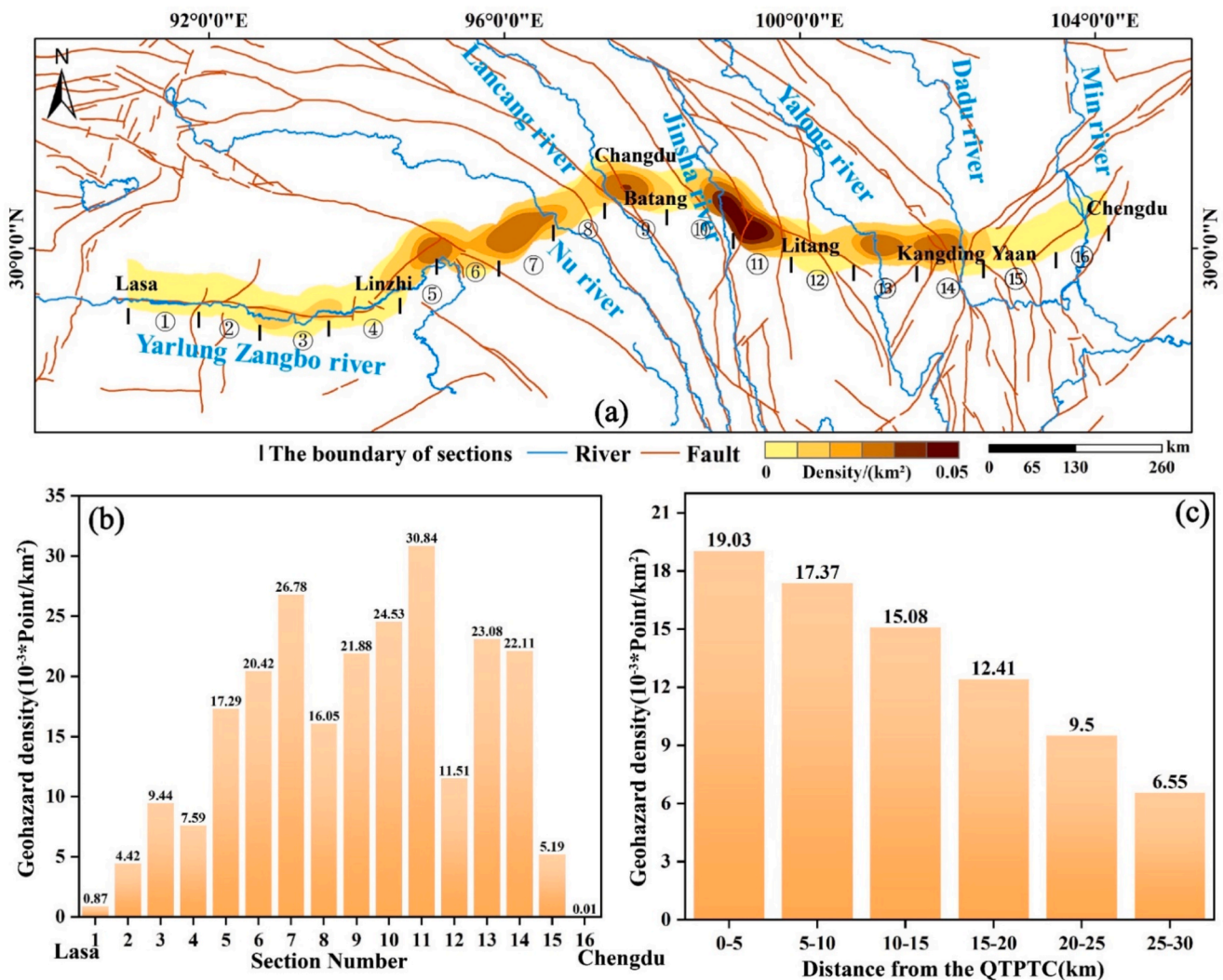
13

Fig. 12. (a) and (b) The geohazard density per section along the QTPTC, (c) geohazard density versus distance along the OTPTC.

displacement time series of P1 and P2 were relatively consistent, and the cumulative deformation reached 57 mm and 34 mm, respectively. In the same period, the deformation trends of P1 and P2 in Fig. 14e and 14 g show good consistency.

The second landslide is a relatively large freeze-and-thaw weathering landslide group (actively deforming slopes) located in Batang County, Sichuan Province, and the distance from this landslide group to the QTPTC is 0.1 km. We divided this landslide group into six freeze-and-thaw weathering landslides (Fig. 15a and 15d). In Fig. 15e and 15f, the LOS surface displacement time series of the pixel point P1 was −58 mm and 21 mm. In Fig. 15e, 15f and 15 g, the pixel point P3 was not deformed before May 2020, and after then, the LOS surface displacement time series reached −49 mm and 25 mm (Fig. 15e and 15f). The upper part of the freeze-and-thaw weathering landslide where P4 is located has a large deformation area, and the LOS surface displacement time series during the monitoring period reached −65 mm, with significant deformation occurring in September 2018 and April 2020 (Fig. 15e). The main deformation areas of the landslide where P5 and P6 are located are distributed on the side of slopes, and the LOS surface displacement time series of the pixel point P5 was −49 mm and 16 mm, and the pixel point P6 was −42 mm and 36 mm (Fig. 15e and 15f). The pixel points P7 and P8 are located at the lower and upper edge of the landslide, respectively, in Fig. 15e, the LOS surface displacement time series of P7 and P8 during the monitoring period were −54 mm and −50 mm. In Fig. 15f, the cumulative deformations of P7 and P8 during the

monitoring period were 58 mm and 61 mm. In Fig. 15e and 15 g, the deformation trend of eight points has a good consistency. Finally, it is worth noting that this landslide group is located near Batang Station of the QTPTC, and long-term monitoring will be required in the future.

5.3. Field survey

To verify the geohazards we detected, three field surveys were conducted, and the period of the first survey was from July 11 to 24, 2020, starting from Chengdu, Sichuan Province, we passed through Xinduqiao, Batang, Baiyu, Changdu, Bashu, Bomi, Bangda, and investigated many typical landslides, for example, Maoyaba landslide (a stabilized historically deformed slope), Baige Landslide (a reactivated historically deformed slope), Xiaomojiu Landslide (an actively deforming slope) and Laigu glacier, and other sites. The second survey was conducted from October 9 to 30, 2020, we started from Chengdu, Sichuan, via Kangding, Litang, Baiyu, Jiangda, Bangda, Ranwu, Lulang, Linzhi, Jiacha, Lasa, and returned to Chengdu finally. In the third field investigation, we focused on some typical demonstration areas from June 30 to July 14, 2021. 141 slopes (48 actively deforming slopes, 38 reactivated historically deformed slopes and 55 stabilized historically deformed slopes) were confirmed, the results of field investigations for those slopes are consistent with the types determined by laboratory analyses, and due to the terrible field environment and weather, the other slopes were not investigated (Fig. 16).
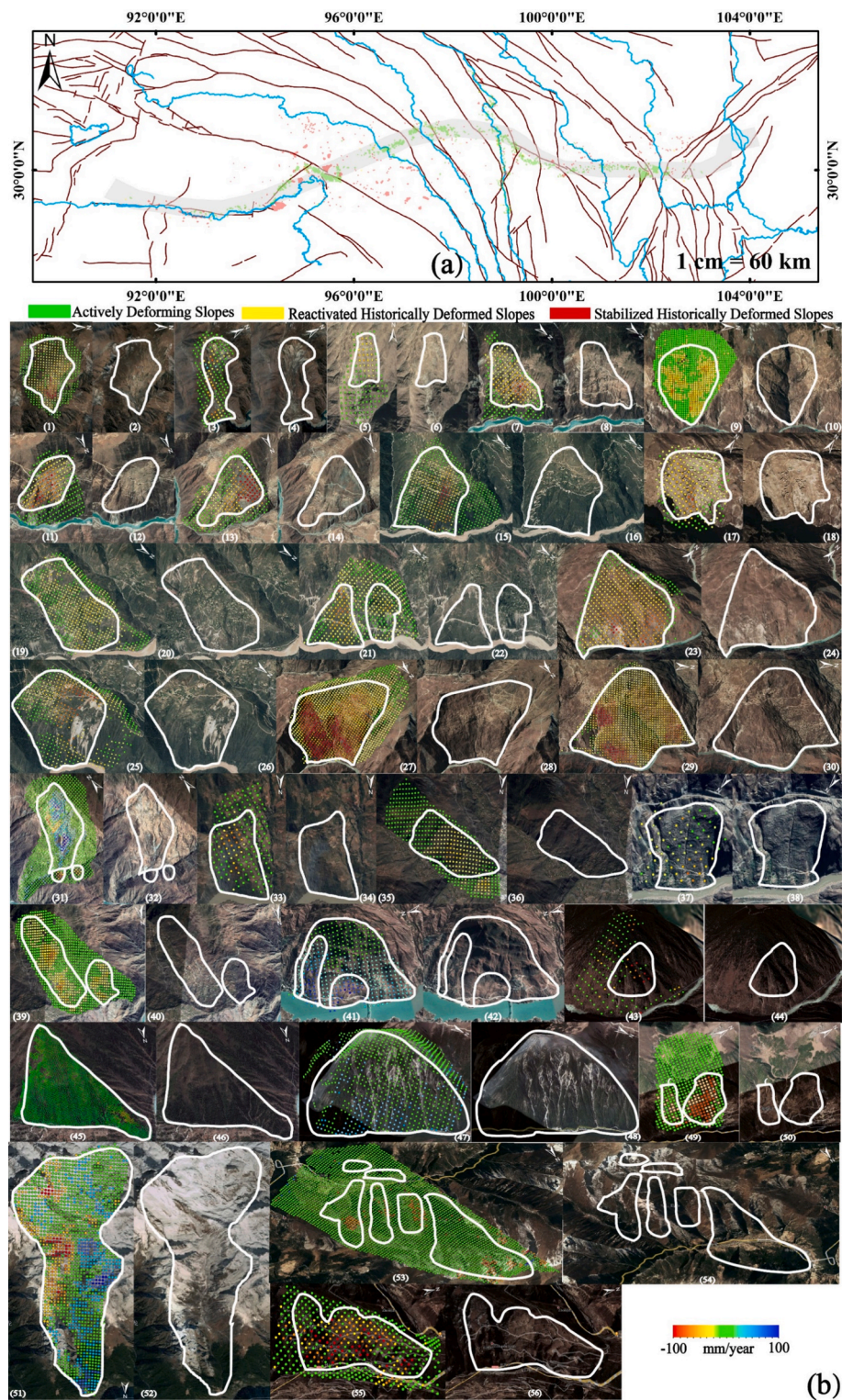
14

Fig. 13. (a) Slopes boundaries. The green indicates actively deforming slopes, the yellow indicates reactivated historically deformed slopes, the red indicates stabilized historically deformed slopes. (b) The mean LOS surface displacement rate maps and optical remote sensing data of 28 typical slopes, the white solid lines mark the boundaries of slopes, and the optical remote sensing images were sourced from Google Earth software.

By field surveys, we verified 141 slopes. Fig. 17a − 17 g show site photographs of Ranwu collapse, Maoyaba landslide, Yigong landslide, Lagang landslide, Baige landslide and Tianmogou debris flow, all of which are historically significant landslides that have occurred in areas near the QTPTC. Ranwu collapse, Maoyaba landslide, Yigong landslide and Lagang landslide were classified as stabilized historically deformed

slopes due to the absence of current deformational information despite possessing characteristic landslide morphological features. And Baige landslide was classified as a reactivated historically deformed slope, exhibiting both ongoing deformational information and distinct landslide morphological features. Fig. 17g and 17 h show site photographs in Fig. 13b − (49), the site investigation revealed that the deformation of
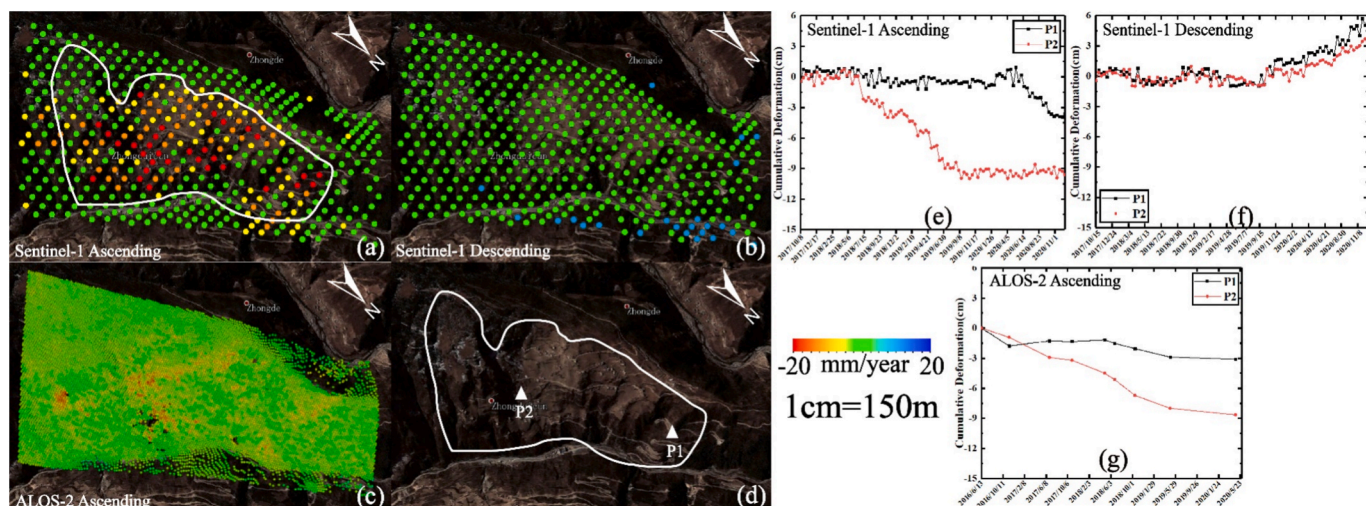
Fig. 14. The mean LOS surface displacement rates: (a) Sentinel-1 ascending, (b) Sentinel-1 descending, (c) ALOS-2 ascending, (d) optical remote sensing image. The LOS surface displacement time series of pixel points P1 and P2: (e) Sentinel-1 ascending, (f) Sentinel-1 descending, and (g) ALOS-2 ascending.
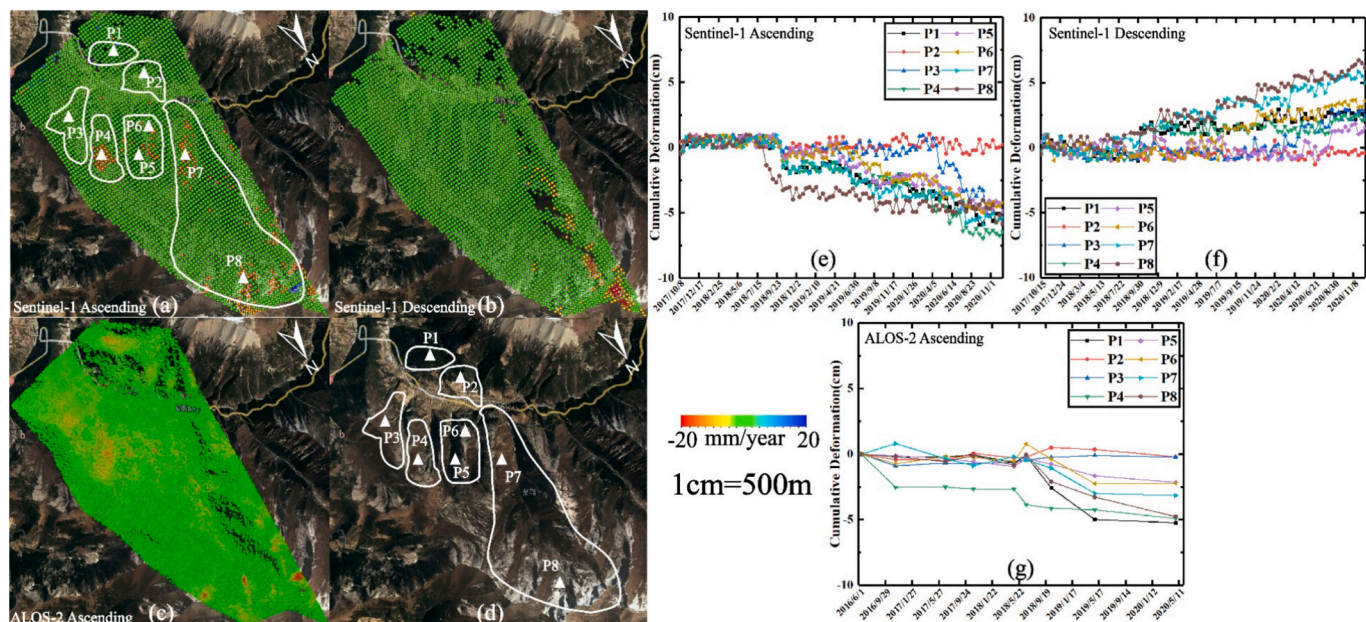

Fig. 15. The mean los surface displacement rate: (a) sentinel-1 ascending, (b) sentinel-1 descending, (c) alos-2 ascending, (d) optical remote sensing image. the los surface displacement time series: (e) sentinel-1 ascending, (f) sentinel-1 descending, and (g) alos-2 ascending.

the area is influenced by mountain roads, with erosion expanding on both sides of the roads, resulting in multiple slides on the surface of this slope (yellow line). Fig. 17j shows a site photograph corresponding to Fig. 14, the slope in this photograph is affected by mountain road construction, resulting in deformation. By observing the site photograph of Fig. 17j (Fig. 14), much dead wood, bent trees and tilted trees are found on the platform where the slope slipped. By estimating the age of trees, it is determined that the slope slid once approximately 10 years ago, and this landslide is finally judged to be a creeping rock landslide.

6. Conclusion

In this study, firstly, to address the issues of omission and misjudgment in identifying potential geohazards within complex hazard-prone environments, high-precision geohazard deformational information was acquired using GACOS-Assisted InSAR and SPOT methods. Concurrently, high-precision geohazard geomorphological information

for the study area was obtained through optical remote sensing visual interpretation. Based on the deformational and geomorphological information of geohazards, the classification theory of geohazards was refined, categorizing them into four distinct types (actively deforming slopes, reactivated historically deformed slopes, stabilized historically deformed slopes and undeformed but potentially unstable slopes collapses). Then, the regularities of geohazards were acquired based on internal factors and surrounding environments of the study area. Finally, we analyzed the influence of geohazards on the QTPTC. The following conclusions are as follows:

1237 active geohazards were detected by GACOS-Assisted InSAR, 36 active geohazards of large gradient surface movements were detected by SPOT, and 1254 geohazards were detected by optical remote sensing, and only 382 geohazards were detected by both SAR and optics remote sensing. Finally, 2109 geohazards were detected in the QTPTC, and they were made a detailed classification and cataloguing according to types of actively deforming slopes (994), reactivated historically deformed
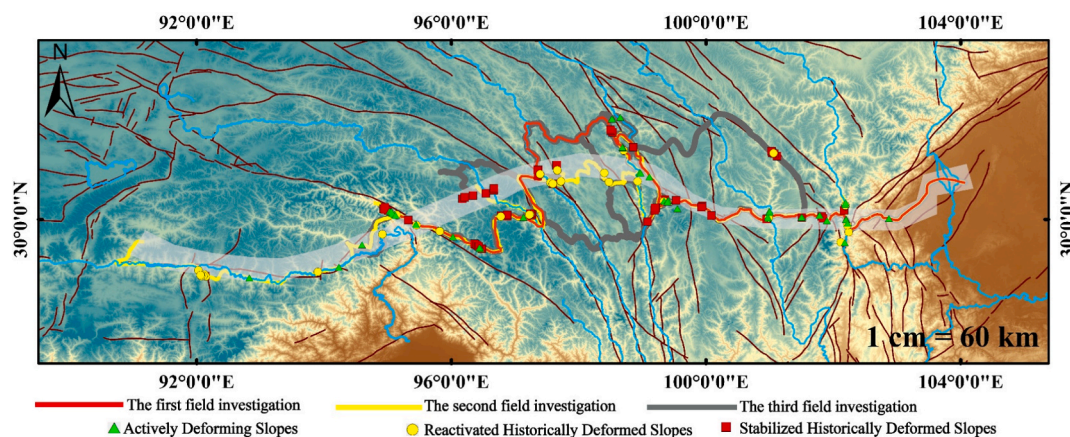
Fig. 16. The routes of three field surveys: the red line indicates the first field survey, the green second field survey, the grey third field survey, and the pink circle indicates landslides confirmed. The green triangle indicates actively deforming slopes, the yellow circle indicates reactivated historically deformed slopes, the red rectangle indicates stabilized historically deformed slopes,

Fig. 17. The site photographs of typical landslides (a-j), (g) and (h): Fig. 12b- (49), (i) and (j): Fig. 13.

slopes (84), stabilized historically deformed slopes (732), glaciers (283) and glacial lakes (16). The highest geohazard density is distributed in the Jinsha River Basin (11th), reaching $30.84*10^{-3}$ points/km^2, and the highest density of 19.03 points/km^2 observed within 5 km of the corridor.

The study area was categorized into five regions according to the spatial distribution of geohazards. Active tectonic zones, river suture zones and lithology within the Tibetan Plateau are the main internal factors of the spatial distribution of geohazards. Five regions with large seismic PGA (>0.2 g) and high seismic activity provide the direct impetus for the occurrence of geohazards. A large percentage of geohazards are distributed at elevation of 2500–5000 m with slope angles of 30-40°, and due to driving factors (precipitation and surface temperature), the types of geohazards in the five regions are varied. Finally, 141 geohazards were verified through field investigations.

The catalogue of 2109 geohazards and the spatial distribution characteristics of geohazards were reported to the construction organization of the QTPTC, there are two geological hazard points that require focused attention, and this study greatly assisted in the engineering design, construction, operation and maintenance. This work could play a significant role in detecting and mapping geohazards, especially in areas with complicated topography, geology and climate conditions, which will be a vital guide for improving the capability of disaster prevention and mitigation during the construction and operation of transportation corridors.

This study addresses the scientific challenges of geohazard detection in complex alpine gorge regions by integrating multi-source remote sensing technologies, thereby overcoming the limitations of single-data-source approaches in detecting geohazards. However, the acquisition of deformational and morphological information relies excessively on manual visual interpretation, resulting in low efficiency that fails to meet the demands for large-scale geohazard detection with frequent updates. In future research, constructing intelligent geohazard identification models will be the primary focus.

CRediT authorship contribution statement

Zhenhong Li: Writing – review & editing, Funding acquisition. **Chenglong Zhang:** Writing – original draft, Software. **Chen Yu:** Writing – review & editing, Validation, Formal analysis. **Mingtao Ding:** Validation, Resources, Investigation. **Wu Zhu:** Supervision, Resources. **Trevor B. Hoey:** Writing – review & editing. **Bo Chen:** Validation, Investigation. **Jiantao Du:** Investigation. **Xinlong Li:** Investigation. **Jianbing Peng:** Supervision.

Declaration of competing interest

The authors declare that they have no known competing financial interests or personal relationships that could have appeared to influence the work reported in this paper.

Acknowledgements

Data availability

Data will be made available on request.

References

Behling, R., Roessner, S., Golovko, D., Kleinschmit, B., 2016. Derivation of long-term spatiotemporal landslide activity- a multi-sensor time series approach. Remote Sens. Environ. 186, 88–104. https://doi.org/10.1016/j.rse.2016.07.017.

Berardino, P., Fornaro, G., Lanari, R., Sansosti, E., 2002. A new algorithm for surface deformation monitoring based on small baseline differential SAR interferograms. IEEE Trans. Geosci. Remote Sens. 40 (11), 2375–2383. https://doi.org/10.1109/TGRS.2002.803792.

Cai, J.H., Zhang, L., Dong, J., Dong, X.J., Li, M.H., Xu, Q., Liao, M.S., 2022. Detection and characterization of slow-moving landslides in the 2017 Jiuzhaigou earthquake area by combining satellite InSAR observations and airborne Lidar DSM. Eng. Geol. 305, 106730. https://doi.org/10.1016/j.enggeo.2022.106730.

Chen, B., Li, Z.H., Song, C., Yu, C., Zhu, W., Liu, Z.J., Han, B.Q., Du, J.T., Zhang, C.L., Xu, F., Peng, J.B., 2024. Automatic detection of active geohazards with millimeter-to-meter-scale deformation and quantitative analysis of factors influencing spatial distribution: a case study in the Hexi corridor, China. Int. J. Appl. Earth Obs. Geoinf. 131, 103995. https://doi.org/10.1016/j.jag.2024.103995.

Chen, B., Li, Z.H., Zhang, C.L., Ding, M.T., Zhu, W., Zhang, S.C., Han, B.Q., Du, J.T., Cao, Y.B., Zhang, C., Liao, Z.Y., Zhou, S.K., Wang, J.W., Peng, J.B., 2022. Wide area detection and distribution characteristics of landslides along Sichuan expressways. Remote Sens. 14 (14), 3431. https://doi.org/10.3390/rs14143431.

Costantini, M., 1998. A novel phase unwrapping method based on network programming. IEEE Trans. Geosci. Remote Sens. 36 (3), 813–821. https://doi.org/10.1109/36.673674.

Cui, P., Ge, Y.G., Li, S.J., Li, Z.H., Xu, X.W., Zhou, G.D., Chen, H.Y., Wang, H., Lei, Y., Zhou, L.B., Yi, S.J., Wu, C.H., Guo, J., Wang, Q., Lan, H.X., Ding, M.T., Ren, J.J., Zeng, L., Jiang, Y.J., Wang, Y., 2022. Scientific challenges in disaster risk reduction for the Sichuan–Tibet Railway. Eng. Geol. 309, 106837. https://doi.org/10.1016/j.enggeo.2022.106837.

Du, J.T., Li, Z.H., Song, C., Zhu, W., Ji, Y.Q., Zhang, C.L., Chen, B., Su, S.R., 2023. InSAR-based active landslide detection and characterization along the upper reaches of the Yellow River. IEEE J. Sel. Top. Appl. Earth Obs. Remote Sens. 16, 3819–3830. https://doi.org/10.1109/JSTARS.2023.3263003.

Fan, Y.K., Ma, P.F., Hu, Q.B., Liu, G.W., Guo, Z.H., Tang, Y.X., Wu, F., Zhang, H., 2025. SCGC-Net: spatial context-guided calibration network for multisource RSI landslides detection. IEEE Trans. Geosci. Remote Sens. 63, 1–17. https://doi.org/10.1109/TGRS.2025.3528750.

Fu, S., Jong, S.M.D., Hou, X.J., Vries, J.D., Deijns, A., Haas, T.D., 2024. A landslide dating framework using a combination of Sentinel-1 SAR and -2 optical imagery. Eng. Geol. 329, 107388. https://doi.org/10.1016/j.enggeo.2023.107388.

Ge, D.Q., Dai, K.R., Guo, Z.C., Li, Z.H., 2019. Early identification of serious geological hazards with integrated remote sensing technologies: thoughts and recommendations. Geomat. Inf. Sci. Wuhan Univ. 44 (7), 949–956. CNKI:SUN: YJJY.0.2019-01-003.

Goldstein, R., Werner, C., 1998. Radar interferogram filtering for geophysical applications. Geophys. Res. Lett. 25, 4035–4038. https://doi.org/10.1029/1998GL900033.

Guo, C.B., Zhang, Y.S., Yang, Z.H., Meng, W., Du, Y.B., 2018. Investigation and Study on active faults and effects of geological hazards along Sichuan-Tibet Railway. Geological Publishing House, Beijing.

Huang, L., Zhen, L., 2011. Comparison of SAR and optical data in deriving glacier velocity with feature tracking. Int. J. Remote Sens. 32 (9–10), 2681–2698. https://doi.org/10.1080/01431161003720395.

Leprince, S., Ayoub, F., Klinger, Y., Avouac, J.P., 2007. Co-registration of optically sensed images and correlation (COSI-Corr): an operational methodology for ground deformation measurements. 2007 IEEE International Geoscience and Remote Sensing Symposium.

Li, Z.H., Fielding, E., Cross, P., 2009. Integration of InSAR time-series analysis and water-vapor correction for mapping postseismic motion after the 2003 bam (Iran) earthquake. IEEE Trans. Geosci. Remote Sens. 47 (9), 3220–3230. https://doi.org/10.1109/TGRS.2009.2019125.

Li, Z.H., Zhang, C.L., Chen, B., Zhan, J.W., Ding, M.T., Lü, Y., Li, X.L., Peng, J.B., 2022. A technical framework of landslide prevention based on multi-source remote sensing and its engineering application. Earth Sci. 47 (6), 1901–1916. https://doi.org/10.3799/dqkx.2022.205.

Othman, A., Gloaguen, R., 2013. Automatic Extraction and Size Distribution of Landslides in Kurdistan Region, NE Iraq. Remote Sens. 5(5): 2389-2410. https://doi.org/10.3390/rs5052389.

Pepe, A., Lanari, R., 2006. On the extension of the minimum cost flow algorithm for phase unwrapping of multitemporal differential SAR interferograms. IEEE Trans. Geosci. Remote Sens. 44, 2374–2383. https://doi.org/10.1109/TGRS.2006.873207.

Shi, X.G., Zhang, L., Balz, T., Liao, M.S., 2015. Landslide deformation monitoring using point-like target offset tracking with multi-mode high-resolution TerraSAR-X data. ISPRS J. Photogramm. Remote Sens. 105, 128–140. https://doi.org/10.1016/j.isprsjprs.2015.03.017.

Singleton, A., Li, Z.H., Hoey, T., Muller, J.P., 2014. Evaluating sub-pixel offset techniques as an alternative to D-InSAR for monitoring episodic landslide movements in vegetated terrain. Remote Sens. Environ. 147, 12. https://doi.org/10.1016/j.rse.2014.03.003.

Strozzi, T., Luckman, A., Murray, T., Wegmuller, U., Werner, C., 2002. Glacier motion estimation using SAR offset-tracking procedures. IEEE Trans. Geosci. Remote Sens. 40 (11), 2384–2391. https://doi.org/10.1109/tgrs.2002.805079.

Sun, G.Q., Guo, B., Zang, W.Q., Huang, X.Z., Han, B.M., Yang, X., Chen, S.T., Wei, C.X., Wu, H.W., 2020. Spatial–temporal change patterns of vegetation coverage in China and its driving mechanisms over the past 20 years based on the concept of geographic division. Geomat. Nat. Haz. Risk 11, 2263–2281. https://doi.org/10.1080/19475705.2020.1837967.

Torres, R., Snoeij, P., Geudtner, D., Bibby, D., Davidson, M., Attema, E., Potin, P., Rommen, B., Floury, N., Brown, M., Traver, I., Deghaye, P., Duesmann, B., Rosich, B., Miranda, N., Bruno, C., L'Abbate, M., Croci, R., Pietropaolo, A., Huchler, M., Rostan, F., 2012. GMES Sentinel-1 mission. Environ. 120, 9–24. https://doi.org/10.1016/j.rse.2011.05.028.

Xu, Q., Zheng, G., Li, W.L., He, C.Y., Dong, X.J., Guo, C., Feng, W.K., 2018. Study on successive landslide damming events of Jinsha River in Baige Village of October 11 and November 3, 2018. J. Eng. Geol. 26 (6), 1534–1551. https://doi.org/10.13544/j.cnki.jeg.2018-406.

Xu, Q., Lu, H.Y., Li, W.L., Dong, X.J., Guo, C., 2022. Types of potential landslide and corresponding identification technologies. Geomat. Inf. Sci. Wuhan Univ. 47 (3), 377–387. https://doi.org/10.13203/j.whugis20210618.

Yagüe-Martínez, N., Prats-Iraola, P., Gonzalez, F., Brcic, R., Shau, R., Geudtner, D., Eineder, M., Bamler, R., 2016. Interferometric processing of Sentinel-1 TOPS data. IEEE Trans. Geosci. Remote Sens. 54, 2220–2234. https://doi.org/10.1109/TGRS.2015.2497902.

Yu, C., Li, Z.H., Penna, N., 2020. Triggered afterslip on the southern Hikurangi subduction interface following the 2016 Kaikōura earthquake from InSAR time series with atmospheric corrections. Remote Sens. Environ. 251, 112097. https://doi.org/10.1016/j.rse.2020.112097.

Yu, C., Penna, N., Li, Z.H., 2017. Generation of real-time mode high-resolution water vapor fields from GPS observations. J. Geophys. Res. Atmos. 122 (2008), 2025. https://doi.org/10.1002/2016JD025753.

Zhang, C.L., Li, Z.H., Yu, C., Chen, B., Ding, M.T., Zhu, W., Yang, J., Liu, Z.J., Peng, J.B., 2022. An integrated framework for wide-area active landslide detection with InSAR observations and SAR pixel offsets. Landslides 19 (12), 2905–2923. https://doi.org/10.1007/s10346-022-01954-z.

Zhang, C.L., Li, Z.H., Yu, C., Song, C., Xiao, R.Y., Peng, J.B., 2021a. Landslide detection of the Jinsha River Region using GACOS assisted InSAR stacking. Geomat. Inf. Sci. Wuhan Univ. 46 (11), 1649–1657. https://doi.org/10.13203/j.whugis20200675.

Zhang, J.M., Zhu, W., Cheng, Y.Q., Li, Z.H., 2021b. Landslide detection in the Linzhi–Ya'an section along the Sichuan–Tibet Railway based on InSAR and hot spot analysis methods. Remote Sens. 13, 3566. https://doi.org/10.3390/rs13183566.

Zhang, L.L., Dai, K.R., Deng, J., Ge, D.Q., Liang, R.B., Li, W.L., Xu, Q., 2021c. Identifying potential landslides by stacking-InSAR in Southwestern China and its performance comparison with SBAS-InSAR. Remote Sens. 13 (18), 3662. https://doi.org/10.3390/rs13183662.

Zhuang, J.Q., Peng, J., Wang, G.H., Javed, J., Wang, Y., Li, W., 2018. Distribution and characteristics of landslide in Loess Plateau: a case study in Shaanxi province. Eng. Geol. 236, 89–96. https://doi. Org/10.1016/j. enggeo.2017.03.001.